COOPERATIVE TRANSPORTATION USING ROTORCRAFT: SWING STATE ESTIMATION AND CONTROL

Elia Costantini[1], Emanuele L. de Angelis[*,2], Fabrizio Giulietti[3]

University of Bologna, Department of Industrial Engineering (DIN), CIRI Aerospace, Forlí, Italy 47121

ABSTRACT

A cooperative transportation scenario is investigated where two rotorcraft carry a suspended payload. First, equations of motion are derived according to the Lagrangian approach, provided the coupled slung–load system is modeled as a set of three point masses and two mass–less rigid cables. It is noted that the system is underactuated, with a residual degree–of–freedom characterizing payload swing motion. An observation model is derived where the oscillation angle is directly obtained from a minimal set of measured information which include the position of both the agents and their acceleration over the local horizontal plane. Data fusion is performed by a recursive algorithm in the form of a Fading Gaussian Deterministic filter, whose theoretical background was recently investigated by one of the authors. Validation is performed in a realistic simulation scenario where multirotors are modeled as rigid bodies in the presence of linear–elastic cables, aerodynamic disturbances, and rotor forces and moments obtained by Blade Element Theory. The estimated swing angle and rate are shown to be suitable feedback variables for payload stabilization tasks. To this end, a control law is proposed to simultaneously perform minimum–swing formation–keeping and trajectory–tracking maneuvers with benefits on flying qualities and overall energy demand.

1. INTRODUCTION

Two approaches are typically envisaged in air delivery scenarios (Ref. 1): the payload can either be rigidly attached to the vehicle or suspended by a cable. The rigid connection represents the most common solution, which consists in the adoption of clamps or a sufficiently large fuselage. As a matter of fact, it leads to increased take–off mass and may be unsuitable for large payloads or on–site operations where landing is not possible (Refs. 2–4). Conversely, payload suspension allows delivering a package without the necessity to land, which improves mission efficiency while preserving rotorcraft performance and simplicity of systems. As a drawback, the payload induces disturbance forces and moments that can significantly affect the motion of the lifting vehicle, which makes the slung–load system underactuated and difficult to be controlled. At the same time, the oscillations may damage the payload or its environment by colliding with obstacles (Ref. 5).

Although the use of a single agent is relatively simple, there are transportation tasks that can be performed only by flexible and scalable multi–agent systems, such as carrying a load heavier than payload capacity of the single vehicle or successfully delivering an object after vehicle failure. To this end, the cooperative transportation solution has been studied in many papers. Based on the control strategy, cable–suspended transportation with formation control can be classified into two groups: UAV–based (decentralized) and payload–based (centralized). In both scenarios, the stabilization of payload oscillations plays a fundamental role, with solutions often derived from literature on overhead crane systems (Ref. 6).

In the decentralized case (Refs. 7–11), the main priority is to maintain the formation of the UAVs while the swing motion is treated as an external disturbance that makes payload position control a challenging task. In Ref. 7, a passivity–based formation control strategy is investigated. It is shown that the interconnected system has a continuum of equilibria and a proof of stability is obtained for all the equilibrium points where the cables are in tension. In Ref. 8, a payload with unknown mass is considered while the formation is subject to wind disturbances. The control structure is analyzed using Lyapunov theory and both simulations and outdoor experiments are presented to further validate the method. A Lyapunov–based controller is introduced in Ref. 9 for aerial co–manipulation of a cable–suspended

[*]Corresponding author
[1]Ph.D. Student, elia.costantini3@unibo.it
[2]Assistant Professor, emanuele.deangelis4@unibo.it
[3]Full Professor, fabrizio.giulietti@unibo.it

payload with two aerial robots. In Ref. 10, a non–linear control strategy based on feedback linearization is used to guide a formation with two UAVs in accomplishing trajectory–tracking tasks, rejecting the load swing, and avoiding obstacles. In Ref. 11, the authors of the present paper propose a controller that allows the agents in the formation to simultaneously perform trajectory–tracking, formation geometry keeping, and payload swing stabilization. The controller is generated for a system made of three point masses and a set of two linear–elastic cables. A proof of local exponential stability is derived with the requirement that the loaded formation exhibits a two–time–scale behavior: the fast dynamics develops with formation geometry stabilization and payload swing damping, while the slow dynamics characterizes the trajectory–tracking task.

In the centralized case (Refs. 12–16), the main priority is trajectory–tracking for the payload. The system is considered to be dynamically coupled, which complicates its controller design. In Ref. 12, the transportation problem is solved by accounting the full dynamics of the system and is inspired by the literature about reconfigurable cable–driven parallel robots. In Ref. 13, a multi–objective controller is designed to carry a point–mass payload by two helicopters with the aim to perform trajectory–tracking, formation geometry keeping, and collision avoidance. In Ref. 14, a sub–optimal LQR–PID controller is suggested to minimize the swing of a point–mass payload by achieving the same velocity for UAVs and payload for a particular formation. In Ref. 15, a hierarchical method is adopted where the payload (defined as the leader) uses knowledge of its current state to determine the net force and moment acting upon its center of gravity, required to follow the desired trajectory. A tension–distribution optimization problem is formulated in a form that is solved using sequential least–squares programming. In Ref. 16, a multi–agent reinforcement learning–based swarm cooperative navigation framework is investigated. A centralized training with decentralized execution approach is adopted with a reward formulation combining negative and positive reinforcements. In order to achieve the desired behavior and reduce the complexity of exploration, training is performed in multiple stages where the difficulty of the swarm goal is gradually increased.

In order to achieve anti–sway capabilities, the estimation of payload position relative to the formation is fundamental. Different solutions are proposed in the literature, where the adoption of optical feedback devices is widespread. Typical methods include the use of motion capture systems, where accuracy comes at the cost of increased complexity, cost, and difficult implementation in real operative scenarios (Ref. 17). In this respect, a compromise solution is represented by the onboard equipment of vision detection systems, although the increased take–off weight, power consumption, computational burden, and sensitivity to environmental conditions represent a drawback (Refs. 18 and 19). Solutions that are not optical–based are suggested in Ref. 20, where an inclinometer attached to the load is used, or in Ref. 21, where potentiometers fixed to the lifting vehicle directly measure the orientation of appendages or suspended rigid links for different manipulation tasks. Also, the adoption of high–accuracy GNSS devices can be envisaged, provided that both the payload and the lifting vehicles are equipped with a dedicated receiver (Ref. 22).

In the present paper a method is proposed to estimate the swing state of a suspended payload cooperatively–transported by two rotorcraft. First, the equations of motion of the coupled slung–load system are derived according to the Lagrangian approach. The obtained model is based on a set of simplifying assumptions that include the description of the lifting vehicles and the load as a point–mass, while cables are assumed to be rigid and mass–less. An ad hoc parametrization of payload position is proposed to characterize the oscillation state and the complete system is shown to be inherently underactuated. The model is linearized about the hovering condition with the payload at rest. An observation algorithm is thus derived to allow the swing angle and rate to be traced back to vehicles' accelerations over the local horizontal plane. The estimation problem is solved recursively according to the Fading Gaussian Deterministic Filter (FGDF), whose theoretical framework allows the identification of the optimal filter configuration that best dampens modeling errors with respect to measurement noise (Ref. 23). In such a way, the globally optimum filter (within its own class) is retrieved, with minimized estimation error. The estimated swing angle and rate are used in a proportional feedback control logic aiming at the stabilization of payload oscillations according to a decentralized formulation. Controller structure, that stems from the idea in Ref. 6, is designed as an auxiliary contribution to available control loops specifically developed for rotorcraft GNC tasks, that include formation geometry keeping, trajectory following, and collision avoidance (Ref. 24). A simple yet effective method is finally presented to estimate payload mass from simple attitude measurements in multirotor applications.

The novelty of the approach is multifold, since: 1) payload swing state is estimated without the need for ad hoc installations or sensors different from the available onboard IMUs; 2) the problem is addressed according to the FGDF method, which makes the estimation less prone to unknown external disturbances and/or non–modeled dynamics, as in Ref. 23; 3) in order to improve filter performance especially in windy conditions as in Ref. 25, a method is proposed to estimate and account the three components of aerodynamic disturbance force acting on each vehicle; 4) the possibility to accurately compute payload mass through simple measurements extends the application field of the cooperative control method to all scenarios where payload mass is not known a priori or varies with time, as in search and rescue, construction, or fire–fighting operations (Ref. 26); 5) the architecture of the proposed controller is suitable for implementation in commercial–off–the–shelf control solutions of wide usage, such as the PX4 standard (Ref. 27); 6) the onboard deployment of recursive algorithm can be eventually performed on one vehicle only with low computational burden, while minimizing the amount of information exchanged between the agents of the formation.

The validity of the method and the performance of the controller are evaluated by numerical simulations in a realistic test case, where a formation made of two octa–rotors is detailed through the description of powerplant components and the blade–element characterization of propellers. Sample maneuvers are proposed for a non–nominal scenario with elastic cables in the presence of environmental disturbances, model uncertainties, and noisy sensor readings. Based on the particular parametrization of problem, the approach is shown to be simple and gives the reader a deep insight into the physical system. The method is of general validity and can be suitably applied to different rotorcraft configurations, showing encouraging advantages in terms of improved flying qualities, safety of operations, and energy efficiency.

2. SYSTEM MODELING

Starting from the definition of reference frames, a 3 degrees–of–freedom mathematical model is adopted to describe both the rotorcraft and the load. After formulating the control problem, numerical validation is performed by considering the i–th multirotor as a rigid body with center of gravity P_i. The vehicles and the suspension cables are assumed to be identical.

2.1. Reference frames

Three right–handed orthogonal reference frames are introduced:

1. an Earth-fixed North-East-Down frame, $\mathcal{F}_E = \{O_E; \boldsymbol{x}_E, \boldsymbol{y}_E, \boldsymbol{z}_E\}$: the origin, O_E, is fixed to a point on the Earth's surface, $\boldsymbol{x}_E$ aims in the direction of geodetic North, $\boldsymbol{z}_E$ points downward along the Earth ellipsoid normal, and $\boldsymbol{y}_E$ completes a right-handed triad. This frame is assumed to be inertial under the assumption of flat and non–rotating Earth;

2. two Body–fixed frames, $\mathcal{F}_{Bi} = \{P_i; \boldsymbol{x}_{Bi}, \boldsymbol{y}_{Bi}, \boldsymbol{z}_{Bi}\}$, $i = 1, 2$. The longitudinal axis $\boldsymbol{x}_{Bi}$ is positive out the nose of the i–th rotorcraft in its selected plane of symmetry, $\boldsymbol{z}_{Bi}$ aims in the direction of fuselage/frame bottom, and $\boldsymbol{y}_{Bi}$ completes a right–handed triad;

3. a rotorcraft structural reference frame, $\mathcal{F}_S = \{O_S; \boldsymbol{x}_S, \boldsymbol{y}_S, \boldsymbol{z}_S\}$, used to locate the center of gravity and all vehicle components: axes are parallel to the body–fixed frame axes, such that $\boldsymbol{x}_S = -\boldsymbol{x}_B$, $\boldsymbol{y}_S = \boldsymbol{y}_B$, and $\boldsymbol{z}_S = -\boldsymbol{z}_B$. Stationlines ($ST$) are measured positive aft along the longitudinal axis. Buttlines (BL) are lateral distances, positive to the right, and waterlines (WL) are measured vertically, positive upward. Without loss of generality, it is assumed that O_S lies on the top surface of multirotor frame and is aligned vertically with multirotor geometric center over the $\boldsymbol{x}_S - \boldsymbol{y}_S$ plane.

A sketch of the i–th rotorcraft including the selected reference frames is reported in Fig. 1.

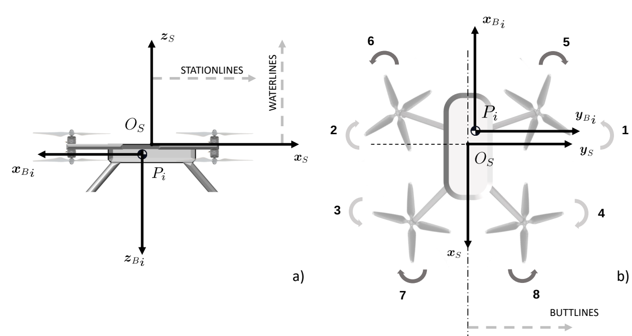

Figure 1: Multirotor body–fixed reference frames

Vector transformation between $\mathcal{F}_E$ and $\mathcal{F}_{Bi}$ is provided by the rotation matrix $\boldsymbol{T}_{BE}(\boldsymbol{\eta}_i)$, where $\boldsymbol{\eta}_i = [\phi_i, \theta_i, \psi_i]^T$ describes the attitude of the i–th rotorcraft through the classical 'roll', 'pitch', and 'yaw' angles, defined by a ZYX Tait–Bryan extrinsic rotation sequence (Refs. 25 and 28). The following notation is adopted: if $\boldsymbol{w}$ is an arbitrary vector, its components are transformed from $\mathcal{F}_E$ to $\mathcal{F}_{Bi}$ through $\boldsymbol{w}_{Bi} = \boldsymbol{T}_{BE}(\boldsymbol{\eta}_i)\,\boldsymbol{w}_E$. In what follows, the subscript E is dropped for simplicity.

2.2. Equations of motion

Let $\boldsymbol{r}_i = [r_{xi}, r_{y_i}, r_{zi}]^T$ be the position of the i–th agent and $\boldsymbol{v}_i = [v_{xi}, v_{y_i}, v_{zi}]^T$ its velocity with respect to the inertial frame. A suspended load with mass m_l is connected in P_l by a cable to the i–th rotorcraft. The dynamics of each agent as expressed in $\mathcal{F}_E$ is described by the following equations:

$$\dot{\boldsymbol{r}}_i = \boldsymbol{v}_i \tag{1}$$

$$\dot{\boldsymbol{v}}_i = \frac{1}{m}\left(m\,\boldsymbol{g} + \boldsymbol{f}_{li} + \boldsymbol{f}_{di} + \boldsymbol{f}_{ci}\right) \tag{2}$$

where m is mass of the rotorcraft, $\boldsymbol{g} = [0,\, 0,\, g]^T$ is local gravitational acceleration vector, $\boldsymbol{f}_{li} = [f_{xl_i},\, f_{yl_i},\, f_{zl_i}]^T$ is the force induced by the load on the i–th rotorcraft through the cable, and $\boldsymbol{f}_{di} = [f_{xd_i},\, f_{yd_i},\, f_{zd_i}]^T$ is vehicle aerodynamic disturbance, that accounts for the contributions of rotorcraft frame drag and rotor in–plane forces. The thrust vector $\boldsymbol{f}_{ci} = [f_{xc_i},\, f_{yc_i},\, f_{zc_i}]^T$, directed along $\boldsymbol{z}_{Bi}$ and pointing upwards, represents the only control input to Eq. (2). It is assumed that the i–th cable is connected to the center of gravity of the i–th agent, such that $\boldsymbol{f}_{li}$ has no effect on attitude motion. Each cable is modeled as mass–less and rigid with constant nominal length L.

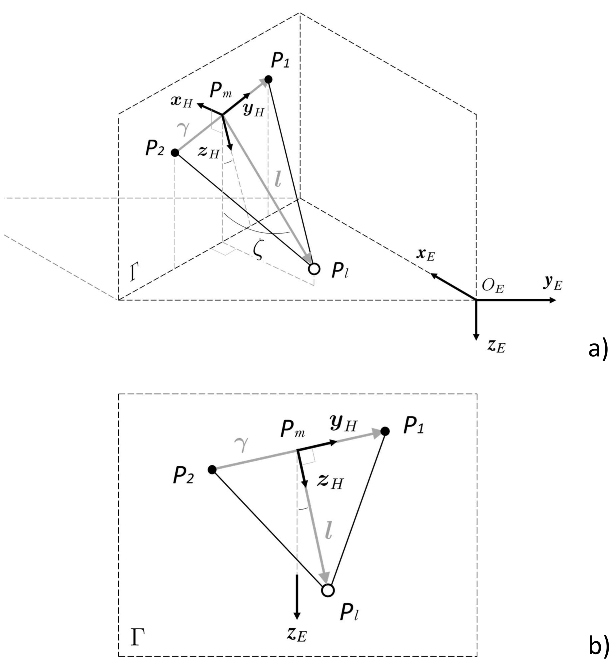

Figure 2: Definition of oscillation angle ζ

With respect to payload position $\boldsymbol{r}_l = [r_{xl},\, r_{yl},\, r_{zl}]^T$, an ad hoc parametrization is adopted which stems from the approach in Ref. 23. Let P_m be the midpoint between P_1 and P_2, with position $\boldsymbol{r}_m = (\boldsymbol{r}_1 + \boldsymbol{r}_2)/2$ (see Fig. 2.a). Define $\boldsymbol{\gamma} = \boldsymbol{r}_1 - \boldsymbol{r}_2$ and $\boldsymbol{\beta} = (\boldsymbol{\gamma}/\gamma) \times \boldsymbol{z}_E$, where $\gamma = \|\boldsymbol{\gamma}\|$ and '$\times$' is the cross–product operator. Consider the reference frame $\mathcal{F}_H = \{P_m; \boldsymbol{x}_H, \boldsymbol{y}_H, \boldsymbol{z}_H\}$ with axes $\boldsymbol{x}_H = \boldsymbol{\beta}/\beta$, $\boldsymbol{y}_H = \boldsymbol{\gamma}/\gamma$, and $\boldsymbol{z}_H = \boldsymbol{x}_H \times \boldsymbol{y}_H = (\boldsymbol{\beta}/\beta) \times (\boldsymbol{\gamma}/\gamma)$, provided $\beta = \|\boldsymbol{\beta}\|$. Note that $\boldsymbol{y}_H$ and $\boldsymbol{z}_H$ lie on the local vertical plane Γ that contains the vehicles, while $\boldsymbol{x}_H$ identifies the plane's normal direction as in Fig. 2.b.

Vector transformation between $\mathcal{F}_H$ and $\mathcal{F}_E$ is provided by rotation matrix $\boldsymbol{T}_{EH} = [\boldsymbol{x}_H \quad \boldsymbol{y}_H \quad \boldsymbol{z}_H]$, where unit vector components are expressed in $\mathcal{F}_E$ as

$$\boldsymbol{x}_H = \left[r_{y_1} - r_{y_2},\, r_{x2} - r_{x1},\, 0\right]^T/\beta \tag{3}$$

$$\boldsymbol{y}_H = \left[r_{x1} - r_{x2},\, r_{y_1} - r_{y_2},\, r_{z1} - r_{z2}\right]^T/\gamma \tag{4}$$

$$\begin{aligned} \boldsymbol{z}_H = \big[&-\left(r_{x1} - r_{x2}\right)\left(r_{z1} - r_{z2}\right), \\ &-\left(r_{y_1} - r_{y_2}\right)\left(r_{z1} - r_{z2}\right), \\ &\left(r_{x1} - r_{x2}\right)^2 + \left(r_{y_1} - r_{y_2}\right)^2\big]^T/\left(\beta\,\gamma\right) \end{aligned} \tag{5}$$

with

$$\beta = \sqrt{\left(r_{x1} - r_{x2}\right)^2 + \left(r_{y_1} - r_{y_2}\right)^2} \tag{6}$$

$$\gamma = \sqrt{\left(r_{x1} - r_{x2}\right)^2 + \left(r_{y_1} - r_{y_2}\right)^2 + \left(r_{z1} - r_{z2}\right)^2} \tag{7}$$

Let $\hat{\boldsymbol{l}} = \boldsymbol{l}/\,\|\boldsymbol{l}\|$ be the unit vector directed from P_m to P_l, where $\boldsymbol{l} = \boldsymbol{r}_l - \boldsymbol{r}_m$ and $\|\boldsymbol{l}\| = \sqrt{L^2 - \gamma^2/4}$ is obtained from simple geometric considerations. Payload position is parametrized through the angle $-\pi/2 < \zeta < \pi/2$, obtained from load rotation about $\boldsymbol{y}_H$. Given $\hat{\boldsymbol{l}} = \boldsymbol{T}_{EH}\,\hat{\boldsymbol{l}}_H$, it is $\hat{\boldsymbol{l}}_H = [\sin\zeta,\, 0,\, \cos\zeta]^T$, such that payload position is calculated as a function of ζ, $\boldsymbol{r}_1$, and $\boldsymbol{r}_2$. It follows:

$$\begin{aligned} \boldsymbol{r}_l &= \boldsymbol{r}_m + \|\boldsymbol{l}\|\;\boldsymbol{T}_{EH}\,[\sin\zeta,\, 0,\, \cos\zeta]^T \\ &= \left(\boldsymbol{r}_1 + \boldsymbol{r}_2\right)/2 \\ &\quad + \left(\sqrt{L^2 - \gamma^2/4}\right)\boldsymbol{T}_{EH}\,[\sin\zeta,\, 0,\, \cos\zeta]^T \end{aligned} \tag{8}$$

Let $\boldsymbol{\lambda} = [\boldsymbol{r}_1^T,\, \boldsymbol{r}_2^T,\, \zeta]^T \in \mathbb{R}^7$ be a vector of generalized coordinates. The Lagrangian equation with respect to $\boldsymbol{\lambda}$ is (Ref. 23):

$$\frac{d}{dt}\left(\frac{\partial E}{\partial \dot{\boldsymbol{\lambda}}}\right) - \frac{\partial E}{\partial \boldsymbol{\lambda}} = \boldsymbol{\tau} \tag{9}$$

where $E = K - U$ is Lagrangian function and $\boldsymbol{\tau} \in \mathbb{R}^7$ is the vector of generalized forces. In the present framework, K is system kinetic energy, given by

$$K = \frac{1}{2}\,m\left(\dot{\boldsymbol{r}}_1^T\dot{\boldsymbol{r}}_1 + \dot{\boldsymbol{r}}_2^T\dot{\boldsymbol{r}}_2\right) + \frac{1}{2}\,m_l\,\dot{\boldsymbol{r}}_l^T\dot{\boldsymbol{r}}_l \tag{10}$$

where $\dot{\boldsymbol{r}}_l$ denotes load velocity as obtained from Eq. (8), namely:

$$\begin{aligned} \dot{\boldsymbol{r}}_l &= \left(\dot{\boldsymbol{r}}_1 + \dot{\boldsymbol{r}}_2\right)/2 \\ &\quad - \frac{\gamma\,\dot{\gamma}}{2\,\sqrt{4\,L^2 - \gamma^2}}\,\boldsymbol{T}_{EH}\,[\sin\zeta,\, 0,\, \cos\zeta]^T \\ &\quad + \left(\sqrt{L^2 - \gamma^2/4}\right)\Big\{\dot{\boldsymbol{T}}_{EH}\,[\sin\zeta,\, 0,\, \cos\zeta]^T \\ &\quad + \boldsymbol{T}_{EH}\,[\cos\zeta,\, 0,\, -\sin\zeta]^T\,\dot{\zeta}\Big\} \end{aligned} \tag{11}$$

With respect to time–derivatives $\dot{\boldsymbol{T}}_{EH}$ and $\dot{\gamma}$ in Eq. (11), it is $\dot{\boldsymbol{T}}_{EH} = [\dot{\boldsymbol{x}}_H \quad \dot{\boldsymbol{y}}_H \quad \dot{\boldsymbol{z}}_H]$, where:

(12) $\dot{\boldsymbol{x}}_H = \big(\dot{\boldsymbol{\beta}}\,\beta - \boldsymbol{\beta}\,\dot{\beta}\big)/\beta^2$

(13) $\dot{\boldsymbol{y}}_H = \big(\dot{\boldsymbol{\gamma}}\,\gamma - \boldsymbol{\gamma}\,\dot{\gamma}\big)/\gamma^2$

(14) $\dot{\boldsymbol{z}}_H = \big[\big(\dot{\boldsymbol{\beta}}\,\beta - \boldsymbol{\beta}\,\dot{\beta}\big)/\beta^2\big] \times \big(\boldsymbol{\gamma}/\gamma\big) + \big[\big(\dot{\boldsymbol{\gamma}}\,\gamma - \boldsymbol{\gamma}\,\dot{\gamma}\big)/\gamma^2\big] \times \big(\boldsymbol{\beta}/\beta\big)$

while

(15) $\dot{\boldsymbol{\beta}} = \big[\dot{r}_{y_1} - \dot{r}_{y_2},\, \dot{r}_{x_2} - \dot{r}_{x_1},\, 0\big]^T$

(16) $\dot{\beta} = \big[\big(\dot{r}_{x_1} - \dot{r}_{x_2}\big)\big(r_{x1} - r_{x2}\big) + \big(\dot{r}_{y_1} - \dot{r}_{y_2}\big)\big(r_{y1} - r_{y2}\big)\big]/\beta$

(17) $\dot{\boldsymbol{\gamma}} = \big[\dot{r}_{x_1} - \dot{r}_{x_2},\, \dot{r}_{y_1} - \dot{r}_{y_2},\, \dot{r}_{z_1} - \dot{r}_{z_2}\big]^T$

(18) $\dot{\gamma} = \big[\big(\dot{r}_{x_1} - \dot{r}_{x_2}\big)\big(r_{x1} - r_{x2}\big) + \big(\dot{r}_{y_1} - \dot{r}_{y_2}\big)\big(r_{y1} - r_{y2}\big) + \big(\dot{r}_{z_1} - \dot{r}_{z_2}\big)\big(r_{z1} - r_{z2}\big)\big]/\gamma$

Potential energy U is related to the vertical displacement of the agents and the suspended load:

(19) $U = -m\,g\,\big(r_{z1} + r_{z2}\big) - m_l\,g\,r_{zl}$

Given the energy contributions in Eqs. (10) and (19) and taking into account the state of the load as described by Eqs. (8) and (11), the Lagrangian equation is manipulated into the system:

(20) $\dot{\boldsymbol{\lambda}} = \boldsymbol{\mu}$

(21) $\boldsymbol{M}(\boldsymbol{\lambda})\,\dot{\boldsymbol{\mu}} + \boldsymbol{C}(\boldsymbol{\lambda}, \boldsymbol{\mu})\,\boldsymbol{\mu} + \boldsymbol{G}(\boldsymbol{\lambda}) = \boldsymbol{\tau}$

where $\boldsymbol{\mu} = [\boldsymbol{v}_1^T, \boldsymbol{v}_2^T, \dot{\zeta}]^T \in \mathbb{R}^7$. For the sake of brevity the highly–nonlinear and lengthy expressions of terms $\boldsymbol{M}(\boldsymbol{\lambda})$, $\boldsymbol{C}(\boldsymbol{\lambda}, \boldsymbol{\mu})$, and $\boldsymbol{G}(\boldsymbol{\lambda})$ are not detailed in the present framework but can be made available to the reader upon request. The generalized force vector $\boldsymbol{\tau} = \boldsymbol{\tau}_c + \boldsymbol{\tau}_d \in \mathbb{R}^7$ is made of a control contribution, $\boldsymbol{\tau}_c$, and a disturbance term, $\boldsymbol{\tau}_d$, that mostly accounts for the aerodynamic drag effects. In particular, it is $\boldsymbol{\tau}_c = [\boldsymbol{f}_{c1}^T, \boldsymbol{f}_{c2}^T, 0]^T$ and $\boldsymbol{\tau}_d = [\boldsymbol{f}_{d1}^T, \boldsymbol{f}_{d2}^T, 0]^T - \boldsymbol{D}\,\boldsymbol{\mu}$, where the latter term accounts for payload drag at low oscillation speed, provided $\boldsymbol{D} = \mathrm{diag}(0, 0, 0, 0, 0, 0, d) \in \mathbb{R}^{7\times 7}$ and $d > 0$ is a drag coefficient.

Remark 1 The constraint on the definition of oscillation angle ζ is considered to avoid singularities in the proposed mathematical representation. In fact, $\boldsymbol{M}(\boldsymbol{\lambda})$ becomes singular if $\zeta = \pm\pi/2$ rad, which occurs when $\hat{\boldsymbol{l}}$ aims in the direction of $\boldsymbol{x}_H$. However, such situation is unlikely to be encountered in practice, provided that aggressive maneuvers or unusual attitudes are not envisaged in safe delivery operations.

3. SWING STATE ESTIMATION

3.1. System linearization

Let $\bar{\boldsymbol{\gamma}} = [\bar{\gamma}_x, \bar{\gamma}_y, 0]^T$ be the prescribed mutual distance vector between the two agents of the formation, with components expressed in $\mathcal{F}_E$, selected such that $\bar{\gamma} = \sqrt{\bar{\gamma}_x^2 + \bar{\gamma}_y^2} < 2\,L$. The system in Eqs. (20) and (21) is linearized about the equilibrium $(\bar{\boldsymbol{y}}, \bar{\boldsymbol{u}})$, where $\bar{\boldsymbol{y}} = [\bar{\boldsymbol{\lambda}}^T, \bar{\boldsymbol{\mu}}^T]^T = [\boldsymbol{r}_1^T, (\boldsymbol{r}_1 - \bar{\boldsymbol{\gamma}})^T, \boldsymbol{0}_{8\times 1}]^T \in \mathbb{R}^{14}$ is representative of a hovering flight condition where the three point–masses lie on the local vertical plane Γ (see Fig. 2), provided the aerodynamic disturbances are a constant, $\bar{\boldsymbol{f}}_{d_1}$ and $\bar{\boldsymbol{f}}_{d_2}$. The term $\bar{\boldsymbol{u}} = [\bar{\boldsymbol{u}}_1, \bar{\boldsymbol{u}}_2]^T \in \mathbb{R}^6$ represents the proper equilibrium force, where $\bar{\boldsymbol{u}}_1 = \bar{\boldsymbol{f}}_{c_1} + \bar{\boldsymbol{f}}_{d_1}$ and $\bar{\boldsymbol{u}}_2 = \bar{\boldsymbol{f}}_{c_2} + \bar{\boldsymbol{f}}_{d_2}$. In such a case $\bar{\zeta} = 0$, $\dot{\bar{\zeta}} = 0$, and vehicle 2 is required to maintain the prescribed position $\bar{\boldsymbol{r}}_2 = \boldsymbol{r}_1 - \bar{\boldsymbol{\gamma}}$. The generalized equilibrium force is obtained as $\bar{\boldsymbol{\tau}} = \bar{\boldsymbol{\tau}}_c + \bar{\boldsymbol{\tau}}_d = \boldsymbol{G}(\bar{\lambda})$. Let $M = 2\,m + m_l$ be the total system mass and define $\xi_i = 2\,(1 - i) + 1$. Taking into account the first 6 components in $\bar{\boldsymbol{\tau}}$, the proper equilibrium force $\bar{\boldsymbol{u}}_i$ is obtained as

(22) $\bar{\boldsymbol{u}}_i = \left[\dfrac{g\,m_l\,\xi_i\,\bar{\gamma}_x}{2\sqrt{4\,L^2 - \bar{\gamma}^2}}, \dfrac{g\,m_l\,\xi_i\,\bar{\gamma}_y}{2\sqrt{4\,L^2 - \bar{\gamma}^2}}, -\dfrac{g\,M}{2}\right]^T$

while the control force generated by the i–th agent is

(23) $\bar{\boldsymbol{f}}_{c_i} = \big[\bar{f}_{x_{c_i}}, \bar{f}_{y_{c_i}}, \bar{f}_{z_{c_i}}\big]^T = \bar{\boldsymbol{u}}_i - \bar{\boldsymbol{f}}_{d_i}$

Theorem 1 *Consider the slung–load system described by Eqs.* (20) *and* (21)*. The equilibrium point* $(\bar{\boldsymbol{y}}, \bar{\boldsymbol{u}})$*, characterized by Eq.* (22) *and obtained by the control force in Eq.* (23)*, satisfies the second–order equation:*

(24) $a_i\,m_l^2 + b_i\,m_l + c_i = 0$

where

(25) $a_i = \dfrac{g^2}{4}\left(\dfrac{\bar{\gamma}^2}{4\,L^2 - \bar{\gamma}^2} - \tan^2\bar{\alpha}_i\right)$

(26) $b_i = -g\left[\xi_i\,\dfrac{\bar{f}_{x_{d_i}}\,\bar{\gamma}_x + \bar{f}_{y_{d_i}}\,\bar{\gamma}_y}{\sqrt{4\,L^2 - \bar{\gamma}^2}} + \big(\bar{f}_{z_{d_i}} + m\,g\big)\tan^2\bar{\alpha}_i\right]$

(27) $c_i = \bar{f}_{x_{d_i}}^2 + \bar{f}_{y_{d_i}}^2 - \big(\bar{f}_{z_{d_i}} + m\,g\big)^2\tan^2\bar{\alpha}_i$

for $i = 1, 2$*, provided* $\bar{\alpha}_i > 0$ *is the angle between* $-\boldsymbol{z}_E$ *and the* i*–th equilibrium control force* $\bar{\boldsymbol{f}}_{c_i}$*. In the case when the agents of the formation are multirotors, it follows* $\bar{\alpha}_i = \arccos(\cos\bar{\phi}_i\,\cos\bar{\theta}_i)$*, provided* $\bar{\boldsymbol{\eta}}_i = [\bar{\phi}_i, \bar{\theta}_i, \bar{\psi}_i]^T$ *is the equilibrium attitude of the* i*–th agent.*

Proof See Appendix 1.

Remark 2 Assume the disturbance force components $\bar{f}_{x_{d_i}}$, $\bar{f}_{y_{d_i}}$, and $\bar{f}_{z_{d_i}}$ are known and the attitude variables $\bar{\phi}_i$ and $\bar{\theta}_i$ are measured in a hovering condition. Eq. (24) can be solved to estimate m_l in all those cases where payload mass is uncertain or not known a–priori. In this respect, an initial hovering maneuver can be envisaged where the formation is stabilized in the desired equilibrium condition and the estimated payload mass $\tilde{m}_l$ is obtained as a steady–state solution to Eq. (24). For values of practical application, two real distinct solutions are obtained, between which the negative one is suitably excluded. The analysis can be performed for either vehicle, nominally leading to the same solution even though different disturbances and attitude variables characterize the multirotors. As an alternative, without loss of generality, agent 1 can be assumed as the formation leader where all necessary information converge to allow any estimation procedures. With respect to the estimation of disturbance forces, different methods are available in the literature, where disturbance observers (DOBs) are typically designed to support the control action in rejecting both external disturbances and effects of model uncertainties (Ref. 29).

Let $\boldsymbol{y} = [\boldsymbol{\lambda}^T, \boldsymbol{\mu}]^T \in \mathbb{R}^{14}$ and $\boldsymbol{u} = [\boldsymbol{u}_1, \boldsymbol{u}_2]^T \in \mathbb{R}^6$ be the state and input vectors respectively describing the dynamics in Eqs. (20)–(21), linearized about the considered equilibrium condition. The standard state–space representation $\dot{\boldsymbol{y}} = \boldsymbol{A}\,\boldsymbol{y} + \boldsymbol{B}\,\boldsymbol{u}$ is obtained where $\boldsymbol{A} \in \mathbb{R}^{14\times14}$ is the state matrix,

$$(28) \quad \boldsymbol{A} = \left[\begin{array}{cccc|c} \multicolumn{4}{c|}{\boldsymbol{0}_7} & \boldsymbol{I}_7 \\ \hline A_{8,1} & A_{8,2} & \dots & A_{8,7} & \\ A_{9,1} & A_{9,2} & \dots & A_{9,7} & \boldsymbol{0}_7 \\ \vdots & \vdots & \ddots & \vdots & \\ A_{14,1} & A_{14,2} & \dots & A_{14,7} & \end{array}\right],$$

and $\boldsymbol{B} \in \mathbb{R}^{14\times6}$ is the input matrix,

$$(29) \quad \boldsymbol{B} = \left[\begin{array}{cccc} \multicolumn{4}{c}{\boldsymbol{0}_{7\times6}} \\ \hline B_{8,1} & B_{8,2} & \dots & B_{8,6} \\ B_{9,1} & B_{9,2} & \dots & B_{9,6} \\ \vdots & \vdots & \ddots & \vdots \\ B_{14,1} & B_{14,2} & \dots & B_{14,6} \end{array}\right]$$

The components of matrices in Eqs. (28) and (29) are detailed in Appendix 2.

3.2. FGDF recursive equations

Let $\boldsymbol{x} = [\zeta, \dot{\zeta}]^T \in \mathbb{R}^2$ be the state vector representing payload oscillation dynamics only. The following linear time–invariant state–space model is extracted from Eqs. (28) and (29):

$$(30) \quad \dot{\boldsymbol{x}} = \boldsymbol{A}_\zeta\,\boldsymbol{x} + \boldsymbol{B}_\zeta\,\boldsymbol{u}$$

where

$$(31) \quad \boldsymbol{A}_\zeta = \begin{bmatrix} 0 & 1 \\ A_{14,7} & 0 \end{bmatrix},$$

and

$$(32) \quad \boldsymbol{B}_\zeta = \begin{bmatrix} 0 & 0 & 0 & 0 & 0 & 0 \\ B_{14,1} & B_{14,2} & B_{14,3} & B_{14,4} & B_{14,5} & B_{14,6} \end{bmatrix}$$

The system in Eq. (30) is reformulated into difference equations where the true state vector $\boldsymbol{x}^{(k)}$ at time k propagates according to $\boldsymbol{x}^{(k+1)} = \boldsymbol{\Phi}^{(k)}\,\boldsymbol{x}^{(k)} + \boldsymbol{\Psi}^{(k)}\,\boldsymbol{u}^{(k)}$. The state transition matrix for the estimation algorithm is obtained as $\boldsymbol{\Phi}^{(k)} = \boldsymbol{\Phi} = \exp(\boldsymbol{A}_\zeta\,\Delta t)$, where $\Delta t = t_{k+1} - t_k$ is the sampling interval. The control–input model is calculated as $\boldsymbol{\Psi}^{(k)} = \boldsymbol{\Psi} = \boldsymbol{A}_\zeta^{-1}(\boldsymbol{\Phi} - \boldsymbol{I}_2)\,\boldsymbol{B}_\zeta$, where $\boldsymbol{I}_2$ is the unit matrix with dimension 2.

The linearization of system dynamics in Eqs. (20)–(21) provides additional information related to vehicles acceleration on the local horizontal plane. For example, the following equation is obtained for agent 1:

$$(33) \quad \boldsymbol{a}_1 = \boldsymbol{\alpha}_1\left[\boldsymbol{r}_1^T, \boldsymbol{r}_2^T\right]^T + \boldsymbol{\beta}_1\,\boldsymbol{u} + \boldsymbol{\lambda}_1\,\zeta$$

where $\boldsymbol{a}_1 = [a_{x_1}, a_{y_1}, a_{z_1}]^T = [\dot{v}_{x_1}, \dot{v}_{y_1}, \dot{v}_{z_1}]^T$ is the acceleration of vehicle 1 as expressed in $\mathcal{F}_E$, provided

$$(34) \quad \boldsymbol{\alpha}_1 = \begin{bmatrix} A_{8,1},\, A_{8,2},\, A_{8,3},\, A_{8,4},\, A_{8,5},\, A_{8,6} \\ A_{9,1},\, A_{9,2},\, A_{9,3},\, A_{9,4},\, A_{9,5},\, A_{9,6} \\ A_{10,1},\, A_{10,2},\, A_{10,3},\, A_{10,4},\, A_{10,5},\, A_{10,6} \end{bmatrix},$$

$$(35) \quad \boldsymbol{\beta}_1 = \begin{bmatrix} B_{8,1},\, B_{8,2},\, B_{8,3},\, B_{8,4},\, B_{8,5},\, B_{8,6} \\ B_{9,1},\, B_{9,2},\, B_{9,3},\, B_{9,4},\, B_{9,5},\, B_{9,6} \\ B_{10,1},\, B_{10,2},\, B_{10,3},\, B_{10,4},\, B_{10,5},\, B_{10,6} \end{bmatrix},$$

and

$$(36) \quad \boldsymbol{\lambda}_1 = \left[A_{8,7},\, A_{9,7},\, 0\right]^T$$

are matrix subsets of $\boldsymbol{A}$ and $\boldsymbol{B}$, with $\boldsymbol{\alpha}_1, \boldsymbol{\beta}_1 \in \mathbb{R}^{3\times6}$, and $\boldsymbol{\lambda}_1 \in \mathbb{R}^{3\times1}$. It is noted from Eqs. (3)–(5) that the ad hoc reference frame $\mathcal{F}_H$ in the equilibrium condition is defined by unit vectors $\bar{\boldsymbol{x}}_H = [\bar{\gamma}_y, -\bar{\gamma}_x, 0]^T/\bar{\gamma}$,

$\bar{\boldsymbol{y}}_H = [\bar{\gamma}_x,\, \bar{\gamma}_y,\, 0]^T/\bar{\gamma}$, and $\bar{\boldsymbol{z}}_H = [0,\, 0,\, 1]^T$. By applying the transformation $\bar{\boldsymbol{T}}_{HE} = \bar{\boldsymbol{T}}_{EH}^T = [\bar{\boldsymbol{x}}_H \quad \bar{\boldsymbol{y}}_H \quad \bar{\boldsymbol{z}}_H]^T$ to both sides of Eq. (33), one obtains

$$(37) \quad \bar{\boldsymbol{T}}_{HE}\left(\boldsymbol{a}_1 - \boldsymbol{\alpha}_1\left[\boldsymbol{r}_1^T,\, \boldsymbol{r}_2^T\right]^T - \boldsymbol{\beta}_1\,\boldsymbol{u}\right) = \begin{bmatrix} \dfrac{g\, m_l}{2\, m}\zeta \\ 0 \\ 0 \end{bmatrix}$$

where the definition of $\boldsymbol{\lambda}_1$ in Eq. (36) is accounted with the values of $A_{8,7}$ and $A_{9,7}$ listed in Appendix 2. Assume that, at time k the input $\boldsymbol{u}^{(k)}$ is known while acceleration $\boldsymbol{a}_1^{(k)}$ and position information $\boldsymbol{r}_1^{(k)}$ and $\boldsymbol{r}_2^{(k)}$ are made available from sensors. Equation (37) thus infers the observability of oscillation angle ζ from acceleration and control contributions along $\boldsymbol{x}_H$ only. Hence, by focusing on the first component, it is possible to obtain a direct measurement ζ_m of swing angle, namely

$$(38) \quad \zeta_m^{(k)} = \frac{2\, m}{g\, m_l}\,\bar{\boldsymbol{x}}_H^T\left(\boldsymbol{a}_1^{(k)} - \boldsymbol{\alpha}_1\left[{\boldsymbol{r}_1^{(k)}}^T,\, {\boldsymbol{r}_2^{(k)}}^T\right]^T - \boldsymbol{\beta}_1\,\boldsymbol{u}^{(k)}\right)$$

The observation $z^{(k)} = \zeta_m^{(k)}$ tracks the considered dynamic process as in $z^{(k)} = \boldsymbol{H}\,\boldsymbol{x}^{(k)}$, where

$$(39) \quad \boldsymbol{H} = \begin{bmatrix} 1 & 0 \end{bmatrix}$$

is the time–invariant observation matrix. The measurements are assumed to be corrupted by noise $\nu^{(k)}$ with variance R, that is

$$(40) \quad z^{(k)} = \boldsymbol{H}\,\boldsymbol{x}^{(k)} + \nu^{(k)}$$

Given the time series of data $z^{(0)}, z^{(1)}, z^{(2)}, \ldots, z^{(k)}$, the aim is to compute estimates in a time series to the state vector, namely $\tilde{\boldsymbol{x}}^{(0)}, \tilde{\boldsymbol{x}}^{(1)}, \tilde{\boldsymbol{x}}^{(2)}, \ldots, \tilde{\boldsymbol{x}}^{(k)}$, by taking into account the model in Eqs. (30)–(32). In what follows, such a problem is solved by a set of Kalman–like recursive equations where the gain matrix is computed through the formal minimization of a cost function, with no other assumption (Ref. 30 and 31). The approach throughly follows the one proposed in Ref. 23, where the Fading Gaussian Deterministic Filter is described in detail and whose same nomenclature is here adopted.

Remark 3 Input $\boldsymbol{u}^{(k)}$ in Eq. (38) is assumed to be known, accounting for both disturbance and control forces. With respect to the knowledge of control force, a sample approximate solution is here provided for a multirotor platform, based on the approach in Ref. 25. Stemming from the definition in Section 2.2, the i–th vehicle control force is expressed as $\boldsymbol{f}_{ci} = -T_i\,\boldsymbol{z}_{Bi} = \boldsymbol{T}_{BE}^T(\boldsymbol{\eta}_i)\,[0,\, 0,\, -T_i]^T$, where T_i is net thrust generated along $\boldsymbol{z}_{Bi}$. Taking into account Eq. (2) and including the estimated external disturbance $\tilde{\boldsymbol{f}}_{d_i}$, the reconstructed thrust magnitude $\tilde{T}_i$ is calculated as

$$(41) \quad \tilde{T}_i = \left\| m\,\boldsymbol{a}_i - m\,\tilde{\boldsymbol{g}} - \tilde{\boldsymbol{f}}_{l_i} - \tilde{\boldsymbol{f}}_{d_i} \right\|$$

where $\tilde{\boldsymbol{g}}$ is measured gravity acceleration and $\tilde{\boldsymbol{f}}_{l_i}$ is the estimated force induced by the load on the i–th multirotor. Under the simplifying assumption that maneuvers are performed near the equilibrium $(\bar{\boldsymbol{y}},\, \bar{\boldsymbol{u}})$, it is possible to assign $m\,\tilde{\boldsymbol{g}} + \tilde{\boldsymbol{f}}_{l_i} \approx -\bar{\boldsymbol{u}}_i$, where $\bar{\boldsymbol{u}}_i$ is retrieved from Eq. (22). Reconstructed control force for filtering purposes is thus $\tilde{\boldsymbol{u}}_i = \boldsymbol{T}_{BE}^T(\tilde{\boldsymbol{\eta}}_i)\,[0,\, 0,\, -\tilde{T}_i]^T$, provided $\tilde{\boldsymbol{\eta}}_i$ is obtained from measured attitude information and $\tilde{T}_i = \left\| m\,\boldsymbol{a}_i + \bar{\boldsymbol{u}}_i - \tilde{\boldsymbol{f}}_{d_i} \right\|$. Note that extension of the proposed method to conventional helicopter configurations can be conceived with minimum effort by accounting for both tail rotor and main rotor contributions in the estimation of net control force.

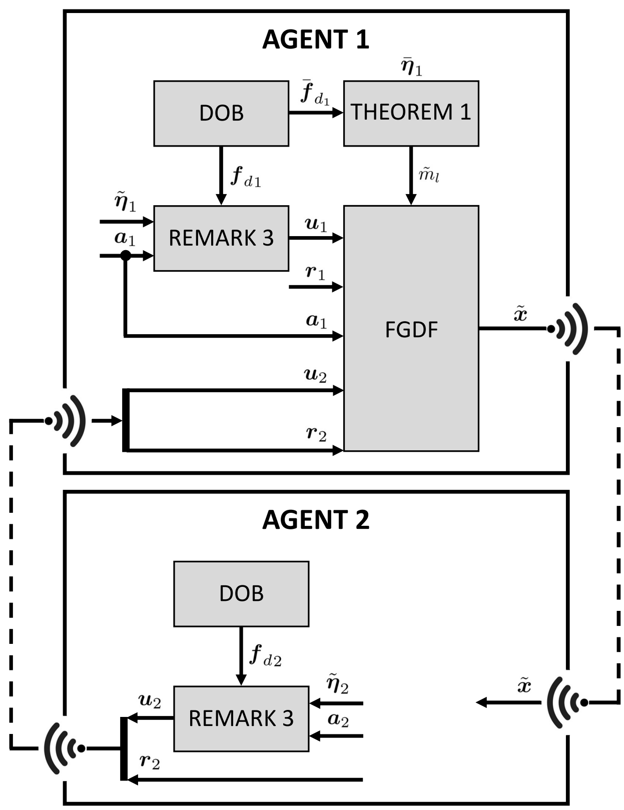

Figure 3: Suitable architecture for FGDF implementation

Fig. 3 suggests a suitable architecture for the implementation of FGDF in a real application scenario. Without loss of generality, Agent 1 is assumed to be the leader, where both payload mass and swing state estimation procedures are computed. On condition that each vehicle is equipped with a DOB, the amount of transmission data is reduced to a minimum, that includes position $\boldsymbol{r}_2$ and reconstructed input force $\boldsymbol{u}_2$ (from agent 2 to agent 1) and estimated swing state $\tilde{\boldsymbol{x}}$ (from agent 1 to agent 2), the latter being available to generate a common payload control action. With respect to the disturbance observation and the control force estimation respectively discussed in Remarks 2 and 3, an alternative method of practical application will be proposed in Section 4, based on the particular control strategy of PX4 standard (Ref. 27).

Table 1: Multirotor slung–load system parameters

Parameter	Symbol	Value	Units
Multirotor			
Mass	m	70	kg
Center of gravity position	$STA_P = BL_P$	0	m
	WL_P	-0.15	m
Moments of inertia	J_{11}	10.61	kg m^2
	J_{22}	10.31	kg m^2
	J_{33}	19.74	kg m^2
	J_{12}	0.037	kg m^2
	J_{13}	-0.043	kg m^2
	J_{23}	-0.003	kg m^2
Center of pressure position	$STA_{CP} = BL_{CP}$	0	m
	WL_{CP}	-0.125	m
Frame drag areas	$A_1 = A_2$	0.22	m^2
	A_3	1.03	m^2
Propeller			
Number of blades	n_b	2	
Radius	R	0.5	m
Mean aerodynamic chord	$\bar{c}$	0.086	m
Chord @ $75\%\,R$	c_{75}	0.103	m
Lift curve slope	a	5.9	rad^{-1}
Pre–cone angle	a_0	0	rad
Root pitch angle	θ_0	0.7854	rad
Total twist	θ_t	-0.6981	rad
Load			
Mass	m_l	100	kg
Reference area	A_l	0.785	m^2
Drag coefficient (sphere)	C_{dl}	0.5	
Cable			
Nominal length	L	15	m
Hooke's constant	K	90 950	N m^{-1}
Damping coefficient	C	215	N m^{-1} s
Hook point position	$STA_H = BL_H$	0	m
	WL_H	-0.2	m

4. RESULTS

4.1. Simulation platform

Simulations are executed in Matlab® environment with a 4th–order Runge–Kutta solver frequency of 500 Hz (Ref. 32). The agents of the formation are two identical octarotors modeled as rigid bodies. The modeling throughly follows the same approach and nomenclature described in Ref. 11, where the selected platform, characterized by a planar set of contra–rotating propellers, is described in detail. For the sake of brevity, only relevant system parameters are listed in Table 1. The payload is assumed to be a point mass attached through a hook point H, distinct from rotorcraft center of gravity. The payload is affected by aerodynamic drag, provided $A_l = \pi R_l^2$ is the frontal area of an equivalent sphere with radius $R_l = 0.5$ m and drag coefficient $C_{dl} = 0.5$. Air parameters are calculated by the International Standard Atmosphere (ISA) model as a function of altitude (Ref. 33). Local gravitational data are provided by the World Geodetic System 1984 model as a function of vehicle latitude, longitude, and altitude (Ref. 34). Let $\boldsymbol{c}_i = \boldsymbol{r}_l - \boldsymbol{r}_i$ be the vector describing the orientation and length of the i–th cable. The force $\boldsymbol{f}_{l\,i}$ in (2) is calculated from the equation

$$(42)\quad \boldsymbol{f}_{l\,i} = \left(K\,\Delta L_i + C\,\Delta\dot{L}_i\right)\hat{\boldsymbol{c}}_i$$

where K is elastic constant, $\Delta L_i = \|\boldsymbol{c}_i\| - L$ and $\Delta\dot{L}_i$ are, respectively, the elastic deformation and its time derivative, and $\hat{\boldsymbol{c}}_i = \boldsymbol{c}_i / \|\boldsymbol{c}_i\|$. With respect to the classical Hookes' model in Ref. 11, cable internal damping is accounted by coefficient C (see Table 1).

4.2. Control system design

In the present Section the control system is designed to fulfill 1) formation–keeping and trajectory–tracking, 2) inter–agent collision avoidance, and 3) active payload stabilization. Control tasks are performed, without loss of generality, through a cascaded algorithm based on PX4 architecture and notation (Ref. 27). The control solution is assumed to stabilize the i–th octarotor according to different flight modes that include the tracking of an Earth–fixed set–point position $\boldsymbol{r}_{sp_i}$, velocity $\boldsymbol{v}_{sp_i}$, or acceleration $\boldsymbol{a}_{sp_i}$ (see Fig. 4, where $\boldsymbol{a}_{sp_i}^{(VC)}$ is the acceleration set–point generated by Velocity Controller).

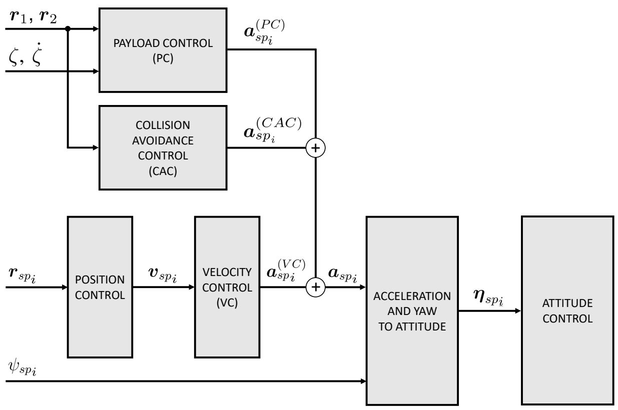

Figure 4: The i–th multirotor control scheme based on PX4 autopilot architecture (Ref. 27)

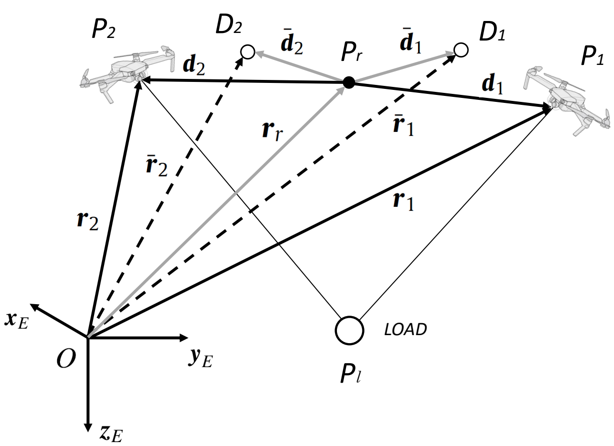

Figure 5: Definition of current (P_i) and desired (D_i) position of the i–th agent

With respect to formation control, assume the i–th vehicle is required to keep a specified distance from a reference point P_r, identified by vector position $\boldsymbol{r}_r(t)$ and moving with velocity $\boldsymbol{v}_r = \dot{\boldsymbol{r}}_r$. Provided D_i is the i–th agent required position, given by $\bar{\boldsymbol{r}}_i$, it is $\boldsymbol{r}_r + \boldsymbol{d}_i = \boldsymbol{r}_i$ and $\boldsymbol{r}_r + \bar{\boldsymbol{d}}_i = \bar{\boldsymbol{r}}_i$, where $\boldsymbol{d}_i = [d_{xi}, d_{y_i}, d_{zi}]^T$ and $\bar{\boldsymbol{d}}_i = [\bar{d}_{x_i}, \bar{d}_{y_i}, \bar{d}_{z_i}]^T$ respectively indicate the current and the required relative distance between the i–th agent and the reference point (see Fig. 5). It is assumed that, when the i–th agent reaches the desired position D_i, the formation midpoint P_m exactly tracks P_r. Based on the definition of $\bar{\gamma}$ in Section 3.1, it follows $\bar{\boldsymbol{d}}_1 = -\bar{\boldsymbol{d}}_2 = [\bar{\gamma}_x/2, \bar{\gamma}_y/2, 0]^T$ and the set–point position in Fig. 4 becomes $\boldsymbol{r}_{sp_i} = \bar{\boldsymbol{r}}_i = \boldsymbol{r}_r + \bar{\boldsymbol{d}}_i$.

Desired acceleration $\boldsymbol{a}_{sp_i} = [a_{sp_{x\,i}}, a_{sp_{y\,i}}, a_{sp_{z\,i}}]^T$ for the i–th multirotor is obtained as

$$(43)\quad \boldsymbol{a}_{sp_i} = \boldsymbol{a}_{sp_i}^{(VC)} + \boldsymbol{a}_{sp_i}^{(CAC)} + \boldsymbol{a}_{sp_i}^{(PC)}$$

where $\boldsymbol{a}_{sp_i}^{(VC)}$ accounts for formation stabilization, $\boldsymbol{a}_{sp_i}^{(CAC)}$ provides collision avoidance capabilities, and $\boldsymbol{a}_{sp_i}^{(PC)}$ implements payload control strategies.

With respect to $\boldsymbol{a}_{sp_i}^{(CAC)}$, the method proposed in Ref. 24 is adopted, based on the definition of potential function

$$(44)\quad V_p(\boldsymbol{\gamma}) = \frac{1}{4}\left[\frac{(\bar{\boldsymbol{\gamma}} - \boldsymbol{\gamma})^T(\bar{\boldsymbol{\gamma}} - \boldsymbol{\gamma})}{\boldsymbol{\gamma}^T\boldsymbol{\gamma} - R_{sph}^2}\right]^2$$

where $R_{sph} < \bar{\gamma}/2$ is the radius of a sphere, centered at P_i, representing a safety zone for the i–th agent. The acceleration contribution allowing for inter–agent collision avoidance is thus:

$$(45)\quad \boldsymbol{a}_{sp_i}^{(CAC)} = \xi_i\, K_a\, \boldsymbol{\nabla} V_p|_{\boldsymbol{\gamma}}$$

where $K_a > 0$ is a control gain and

$$(46)\quad \boldsymbol{\nabla} V_p|_{\boldsymbol{\gamma}} = -\frac{(\bar{\boldsymbol{\gamma}} - \boldsymbol{\gamma})\,\|\bar{\boldsymbol{\gamma}} - \boldsymbol{\gamma}\|^2}{\left(\boldsymbol{\gamma}^T\boldsymbol{\gamma} - R_{sph}^2\right)^2} - \frac{\boldsymbol{\gamma}\,\|\bar{\boldsymbol{\gamma}} - \boldsymbol{\gamma}\|^4}{\left(\boldsymbol{\gamma}^T\boldsymbol{\gamma} - R_{sph}^2\right)^3}$$

is the gradient of potential function in Eq. (44) with respect to γ. In the present case, it is $R_{sph} = 2$ m and $K_a = 0.05$ m^2/s^2.

The proposed payload controller is structured as

$$(47)\quad \boldsymbol{a}_{sp_i}^{(PC)} = \left(k_p\,\zeta + k_d\,\dot{\zeta}\right)\boldsymbol{x}_H,$$

being directed over the local horizontal plane in the direction of $\boldsymbol{x}_H$, where k_p and k_d are positive gains and ζ and $\dot{\zeta}$ are estimated through the FGDF. In the present framework, it is $k_p = 9$ m/(rad s^2) and $k_d = 2$ m/(rad s).

Remark 4 The detailed analysis of PX4 control functions and rotorcraft capability to track a setpoint acceleration are out of the scope of the present paper. In a general perspective, different control strategies can be designed to perform attitude control and generate the required thrust, that include standard PID techniques (Ref. 35), linear quadratic regulators (Ref. 36), active disturbance rejection controllers (Ref. 37), backstepping control or feedback linearization (Ref. 38), and sliding mode methods (Refs. 39 and 40).

4.3. Available measurements

Non–ideal sensing behavior is considered where noise, bias, and sensor positioning errors are introduced and described from a numerical standpoint. Onboard computer is located in $STA_{PIX} = BL_{PIX} = 0$ m and $WL_{PIX} = -0.1$ m, with axes aligned with $\mathcal{F}_B$–axes. To simulate the effects of sensor noise, zero–mean Gaussian white noise is added to each Euler angle and angular velocity measurement, with standard deviations $\sigma_\alpha = 0.018$ deg and $\sigma_\omega = 0.095$ deg/s, respectively. The body–fixed accelerometer readings are obtained by adding white Gaussian noise with $\sigma_{acc} = 0.015$ m/s^2 and constant bias $\boldsymbol{b}_{acc_1} = [0.015, -0.01, 0.002]^T$ m/s^2

and $\boldsymbol{b}_{acc_2} = [-0.004,\, 0.007,\, -0.02]^T$ m/s^2 to the simulated values of vehicle 1 and 2, respectively. Estimation error is also considered for vehicle position and velocity expressed in $\mathcal{F}_E$, provided standard deviations $\sigma_p|_{xy} = 0.074$ m and $\sigma_v|_{xy} = 0.009$ m/s affect the motion over the local–horizontal plane, while $\sigma_p|_z = 0.034$ m and $\sigma_v|_z = 0.005$ m/s characterize the vertical channel. The onboard computer operates at a frequency of 100 Hz (sample time $\Delta t = 0.01$ s) and a fixed time delay, $t_d = 0.04$ s, is implemented to account for local processing and communication issues between the agents of the formation. Note that, among all broadcast signals, the reference trajectory information (provided, for example, by a ground control station) must be included. Same consideration holds for the mutual transmission of agent position data to reconstruct the $\boldsymbol{x}_H = \boldsymbol{x}_H(\boldsymbol{r}_1,\, \boldsymbol{r}_2)$–term in Eq. (47).

Based on the particular control strategy of PX4 standard in Fig. 4, a simple yet effective method is adopted to compute the input force $\boldsymbol{u}_i = \boldsymbol{f}_{ci} + \boldsymbol{f}_{di}$. Assuming ideal electric motors, the thrust value is derived as $\tilde{T}_i = m\,\|\boldsymbol{a}_{sp_i}\|$. By accounting for attitude dynamics, the generated control force as expressed in $\mathcal{F}_E$ is estimated $\tilde{\boldsymbol{f}}_{c_i} = \boldsymbol{T}^T_{BE}(\tilde{\boldsymbol{\eta}}_i)\,[0,\, 0,\, -\tilde{T}_i]^T$. With respect to the analysis of external disturbances, it is noted that velocity controller in Fig. 4 is based on a simple PID implementation (Ref. 27), where the error between the set–point and the measured velocity is transformed into the desired acceleration $\boldsymbol{a}^{(VC)}_{sp_i} = \boldsymbol{a}^{(VC)}_{sp_i}\Big|_P + \boldsymbol{a}^{(VC)}_{sp_i}\Big|_I + \boldsymbol{a}^{(VC)}_{sp_i}\Big|_D$, where the subscripts 'P', 'I', and 'D' respectively denote the proportional, integral, and derivative contributions. Under the hypothesis of quasi–steady external disturbances, based on the capability of integral contributions to reject external disturbances (Ref. 41), it is assumed that $\tilde{\boldsymbol{f}}_{d_i} = -m\;\boldsymbol{a}^{(VC)}_{sp_i}\Big|_I$. Hence, estimated input force is given as $\hat{\boldsymbol{u}}_i = \boldsymbol{T}^T_{BE}(\tilde{\boldsymbol{\eta}}_i)\,[0,\, 0,\, -\tilde{T}_i]^T - m\;\boldsymbol{a}^{(VC)}_{sp_i}\Big|_I$.

4.4. *Performance indicators*

Indicators are defined with the aim to quantitatively characterize the performance of the closed–loop system with and without the auxiliary support of PC.

- Maneuver time, t_m. It is the total time required to conclude the considered maneuver, based on a stop criterion. Define $\boldsymbol{\delta}_i = [\delta_{xi},\, \delta_{y_i},\, \delta_{zi}]^T = \bar{\boldsymbol{d}}_i - \boldsymbol{d}_i$ and $\boldsymbol{\epsilon}_i = [\epsilon_{xi},\, \epsilon_{y_i},\, \epsilon_{zi}]^T = \boldsymbol{v}_r - \boldsymbol{v}_i$ as the relative position and trajectory error variables, respectively. The simulation starts at $t = 0$ s and is assumed to be concluded when two conditions are simultaneously satisfied: 1) the formation control residual error $e_r = \left\|[\boldsymbol{\delta}_1^T\, \boldsymbol{\epsilon}_1^T\, \boldsymbol{\delta}_2^T\, \boldsymbol{\epsilon}_2^T]\right\|$ falls below 0.2, provided $\boldsymbol{\delta}_i$ and $\boldsymbol{\epsilon}_i$ are expressed in m and m/s, respectively, and 2) the absolute value of ζ remains bounded below 0.5 deg for a prescribed time of 5 s.

- Average swing angle, ζ_{av}. It is calculated as $\zeta_{av} = I_\zeta(t_m)/t_m$ where the integral

$$I_\zeta(t_m) = \int_0^{t_m} |\zeta(s)|\, ds \tag{48}$$

  is evaluated over maneuver time interval and provides an indication of how much and how long payload position P_l remains far from the local vertical plane Γ.

- Total propulsive energy, E_{prop}. It is the mechanical energy delivered by electrical motors to propellers, calculated by the integral

$$E_{prop} = \int_0^{t_m} \sum_{j=1}^{8} P_{shj}(s)\, ds \tag{49}$$

  where $P_{shj} = Q_j\, \Omega_j$ is the output shaft power generated by the j–th motor, $j = 1, \ldots, 8$, obtained from required torque Q_j and angular rate Ω_j under the assumption of null friction torque. In the present case, E_{prop} is calculated for agent 1.

4.5. *Test cases*

Consider the desired formation identified by $\bar{\boldsymbol{\gamma}} = [0,\, 10,\, 0]^T$ m. It follows $\bar{\boldsymbol{d}}_1 = -\bar{\boldsymbol{d}}_2 = [0,\, 5,\, 0]^T$ m, provided $\bar{\gamma}_x = 0$ m and $\bar{\gamma}_y = 10$ m.

The first simulation case ('1') is described to validate the formation acquisition capabilities and the payload mass estimation method discussed in Theorem 1 and Remark 2 while $\boldsymbol{a}^{(PC)}_{sp_i} = \boldsymbol{0}$ m/s^2. The octarotors are required to leave the initial state defined at $t = 0$ s by $\boldsymbol{r}_1(0) = [2,\, 5.2,\, -18]^T$ m, $\boldsymbol{r}_2(0) = [-4,\, -5.2,\, -18]^T$ m, and $\boldsymbol{v}_1(0) = \boldsymbol{v}_2(0) = [0,\, 0,\, 0]^T$ m/s, with $\zeta(0) = 3.6$ deg and $\dot{\zeta}(0) = 0$ deg/s. The initial attitude is represented by $\boldsymbol{\eta}_1(0) = -\boldsymbol{\eta}_2(0) = [8.89,\, -5.19,\, 0]$ deg. The reference point is a constant, $\boldsymbol{r}_r(t) = [0,\, 0,\, -20]^T$ m, and the desired yaw angle is $\psi_{sp_1} = \psi_{sp2} = 0$ deg. The maneuver is performed in the presence of a constant wind $\boldsymbol{w} = [-2,\, 1.5,\, 0]^T$ m/s, with components expressed in $\mathcal{F}_E$. During the maneuver, performed with a prescribed 60 s duration, Eq. (24) is solved onboard vehicle 1 and the solution $\hat{m}_l = (-b_1 + \sqrt{b_1^2 - 4\,a_1\,c_1})/(2\,a_1)$ is considered.

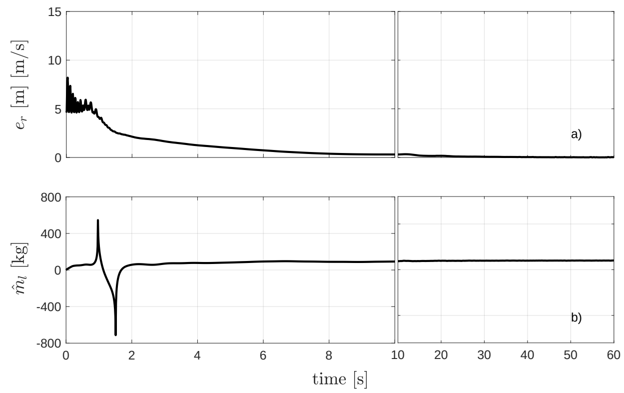

Figure 6: Case 1: (a) stabilization of formation error, (b) static estimation of payload mass

In Fig. 6.a, the residual error e_r is plotted as a function of time, showing correct stabilization of formation geometry. In Fig. 6.b, the estimated payload mass is reported, provided a low–pass filter is applied to the computed value, as obtained by a first–order transfer function with time constant $\tau_{LP} = 0.5$ s. After a rapid initial transient ($t \leq 2$ s), the algorithm reaches plausible values and then stabilizes to a steady–state solution. By averaging the last 10 s of data, one has $\hat{m}_l = 99.76$ kg, which infers satisfactory accuracy. It is noted that the estimation error (-0.24%) mostly accounts for the presence of a hook point that is distinct from vehicle's center of gravity, which goes against the hypotheses at the basis of proposed algorithms (and is responsible for the high–frequency oscillations in Figs. 6–8).

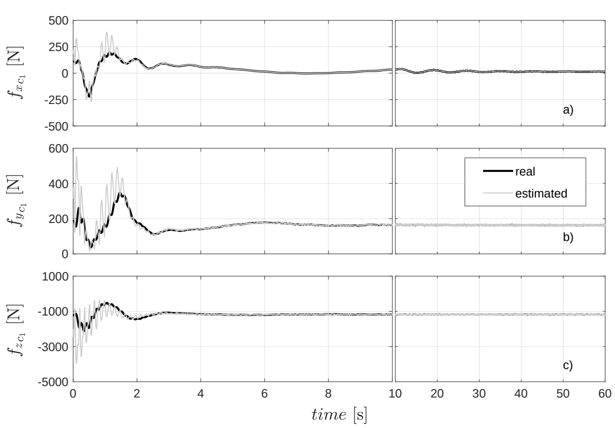

Figure 7: Case 1: comparison between real and estimated control forces

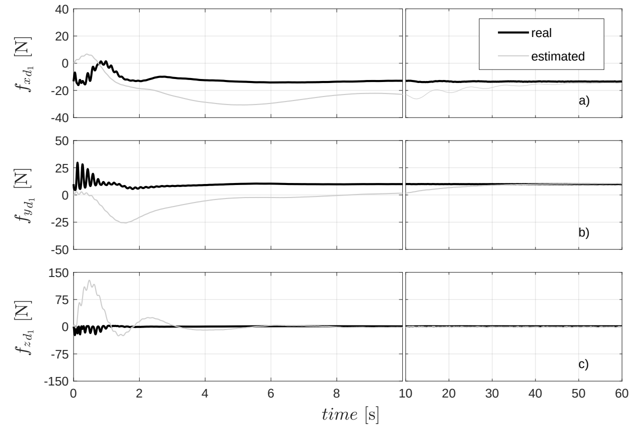

Figure 8: Case 1: comparison between real and estimated disturbance forces

The estimation of control and disturbance forces plays a fundamental role, as it was pointed out in Remark 2. In this respect, Figs. 7 and 8 report a comparison between real and estimated values for vehicle 1, which reaches the steady–state measured attitude identified by $\bar{\phi}_1 = 7.88$ deg, $\bar{\theta}_1 = -0.71$ deg, and $\bar{\alpha}_1 = \arccos(\cos\bar{\phi}_1 \cos\bar{\theta}_1) = 7.91$ deg. During the maneuver payload oscillations are excited according to Fig. 9, until the rest condition is practically acquired. The system results to be evidently underdamped, provided dissipative effects are related only to payload drag and to the stabilization of formation speed errors, $\boldsymbol{\epsilon}_1$ and $\boldsymbol{\epsilon}_2$.

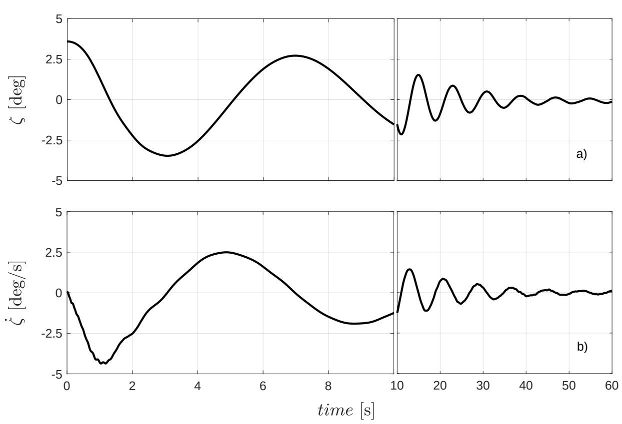

Figure 9: Case 1: stabilization of swing angle and rate

The second maneuver ('2') is adopted as a test case to perform filter tuning, based on payload mass value $\hat{m}_l$ estimated above. The octarotors leave the initial state defined by $\boldsymbol{r}_1(0) = [0,\, 5,\, -20]^T$ m, $\boldsymbol{r}_2(0) = [0,\, -5,\, -20]^T$ m, and $\boldsymbol{v}_1(0) = \boldsymbol{v}_2(0) = [0,\, 0,\, 0]^T$ m/s, with the payload at rest in the absence of wind. The initial attitude is given by $\boldsymbol{\eta}_1(0) = -\boldsymbol{\eta}_2(0) = [8.38,\, 0,\, 0]$ deg. The reference point is a constant, $\boldsymbol{r}_r(t) = [20,\, 0,\, -20]^T$ m, and the desired yaw angle is $\psi_{sp_1} = \psi_{sp_2} = 0$ deg. Dynamic system matrices in Eqs. (31)

and (32) are, respectively:

$$\boldsymbol{A}_{\zeta} = \begin{bmatrix} 0 & 1 \\ -1.1876 & 0 \end{bmatrix} \tag{50}$$

and

$$\boldsymbol{B}_{\zeta} = \begin{bmatrix} 0 & 0 & 0 & 0 & 0 & 0 \\ -0.5051 & 0 & 0 & -0.5051 & 0 & 0 \end{bmatrix} \cdot 10^{-3} \tag{51}$$

The state–transition matrix is computed by Matlab® matrix exponential function $expm(\cdot)$, according to the method in Ref. 42:

$$\boldsymbol{\Phi} = \begin{bmatrix} 0.9999 & 0.010 \\ -0.0119 & 0.9999 \end{bmatrix} \tag{52}$$

The control–input model is:

$$\boldsymbol{\Gamma} = \begin{bmatrix} -0.0025 & 0 & 0 & -0.0025 & 0 & 0 \\ -0.5051 & 0 & 0 & -0.5051 & 0 & 0 \end{bmatrix} \cdot 10^{-5} \tag{53}$$

For the sake of brevity, the tuning and scaling procedures detailed in Ref. 23 to find the globally–optimum FGDF configuration are not described. Final results are directly provided, where $\beta = 0.998$ is the best fading factor at which the estimated measurement noise covariance matrix $\tilde{R}$ satisfies $\tilde{R} = R^{\star} \approx R$, where $R^{\star}$ and R are, respectively, the assigned and the true noise covariance values. In the present case $R = 1.98 \cdot 10^{-5}$ rad^2 and the assigned value is $R^{\star} = 1.95 \cdot 10^{-5}$ rad^2. The algorithm is initialized with null state vector and nominal error covariance $(\boldsymbol{E}^{-})^{(0)} = \mathrm{diag}(8, 9) \cdot 10^{-8}$. The time history of formation residual e_r in the case when $\boldsymbol{a}_{sp_i}^{(PC)} = \boldsymbol{0}$ m/s^2 is reported in Fig. 10.a, provided that maneuver time is $t_m = 71.2$ s. Filter stabilization occurs as in Fig. 10.b, where the trace of the nominal covariance matrix $\boldsymbol{E}$ (and, therefore, the gain of the estimator) sets on a constant value. With respect to filter performance, a comparison is reported in Fig. 11 between the true, the filter–estimated, and the measured oscillation angle according to Eq. (38). In Fig. 12 satisfactory performance of the recursive algorithm is assessed also for the estimation of oscillation rate.

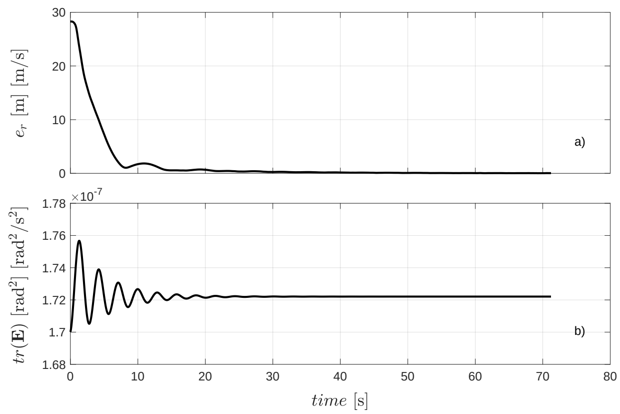

Figure 10: Case 2: (a) formation error stabilization and (b) estimation convergence for the nominal covariance matrix

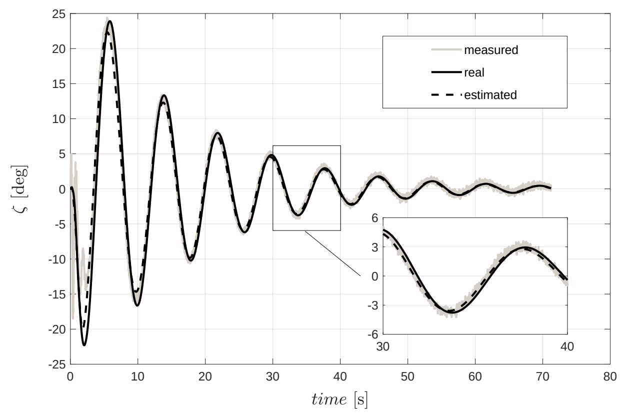

Figure 11: Case 2: comparison between the real, the measured, and the estimated oscillation angle

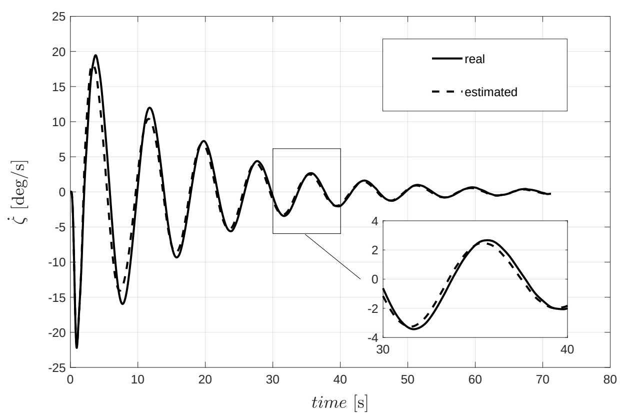

Figure 12: Case 2: comparison between the real and the estimated oscillation rate

In the case when PC is activated according to Eq. (47), based on the feedback of estimated variables, the same maneuver is concluded with $t_m = 42.1$ s. The beneficial effect of $\boldsymbol{a}_{sp_i}^{(PC)}$ is evident in Fig. 13, where the oscillation variables are shown to be rapidly damped. With respect to other performance indicators, Table 2 summarizes main results and computes percentage errors. Among the considered variables, it is noteworthy that a 40.8% reduction of required energy is obtained thanks to PC strategy.

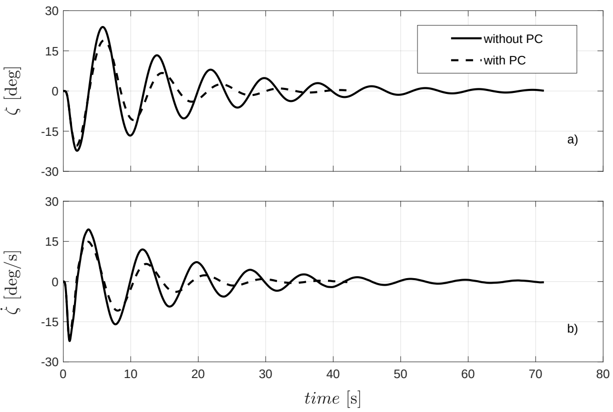

Figure 13: Case 2: stabilization of oscillation (a) angle and (b) rate with and without PC

Table 2: Case 2: summary of performance indicators

index	without PC	with PC	error [%]
t_m [s]	71.2	42.1	-40.9
$I_\zeta(t_m)$ [deg s]	299.71	172.03	-42.6
ζ_{av} [deg]	4.21	4.08	-3.1
E_{prop} [kJ]	995.7	589.6	-40.8

In the last simulation case ('3') the octarotors start from a hovering condition characterized by $\boldsymbol{r}_1(0) = [2,\,0,\,-20]^T$ m and $\boldsymbol{r}_2(0) = [-2,\,0,\,-20]^T$ m with the payload at rest in the presence of steady wind $\boldsymbol{w} = [-0.5,\,2,\,-1]^T$ m/s. Desired formation geometry and FGDF equations are reconfigured to $\bar{\boldsymbol{\gamma}} = [4,\,0,\,0]^T$ m, with null set–point yaw angles. The tuning, scaling, and initialization parameters given above for the estimation algorithm are left unchanged to validate filter configuration robustness with respect to (at least bounded) formation geometry variations. Reference trajectory is defined by $\boldsymbol{r}_r(t) = [t,\,2,\,-20]^T$ m ($\boldsymbol{v}_r(t) = [1,\,0,\,0]^T$ m/s) for $t < 20$ s and $\boldsymbol{r}_r(t) = [2\,t - 20,\,0,\,-20]^T$ m ($\boldsymbol{v}_r(t) = [2,\,0,\,0]^T$ m/s) for $t \geq 20$ s. An additive disturbance signal $\boldsymbol{a}_{sp_1}^{(D)} = [-3,\,0,\,0]^T$ m/s^2 is assumed to perturb Eq. (43) for $i = 1$ during time interval $30 \leq t \leq 31$ s, thus simulating a short–term malfunction of control system in agent 1. Provided the focus is posed on speed tracking capabilities, Condition 1 in Section 4.4, that defines maneuver time, is here adapted to the reduced–order speed error $e_{rs} = \left\|[\boldsymbol{\epsilon}_1^T,\,\boldsymbol{\epsilon}_2^T]\right\|$, required to fall below 0.02 m/s. Fig. 14.a reports the time history of error $e_\gamma = \|\bar{\boldsymbol{\gamma}} - \boldsymbol{\gamma}\|$, showing stabilization of close formation for $R_{sph} = 1$ m. The beneficial effect of CAC is evident during time interval $30 \leq t \leq 31$ s (see gray areas), where safety margin with respect to eventual collisions is guaranteed. In Fig. 14.b, the speed error e_{rs} is plotted with satisfactory accuracy of the speed–tracking capabilities. Table 3 resumes main indicator values with evident advantages of the proposed estimation and control strategy, especially in terms of required energy and maneuver time. Finally, Fig. 15 depicts the true oscillation angle and rate as obtained with and without PC, showing reduced swing in the former case.

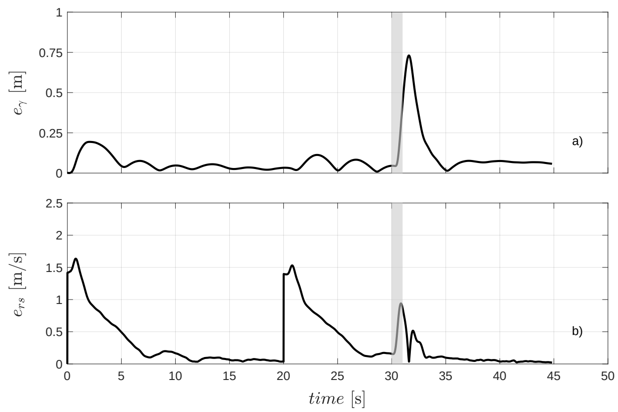

Figure 14: Case 3: stabilization of (a) formation geometry and (b) residual speed error with PC

Table 3: Case 3: summary of performance indicators

index	without PC	with PC	error [%]
t_m [s]	60.4	44.8	-25.7
$I_\zeta(t_m)$ [deg s]	62.60	34.76	-44.5
ζ_{av} [deg]	1.04	0.78	-25.2
E_{prop} [kJ]	845.6	630.5	-25.4

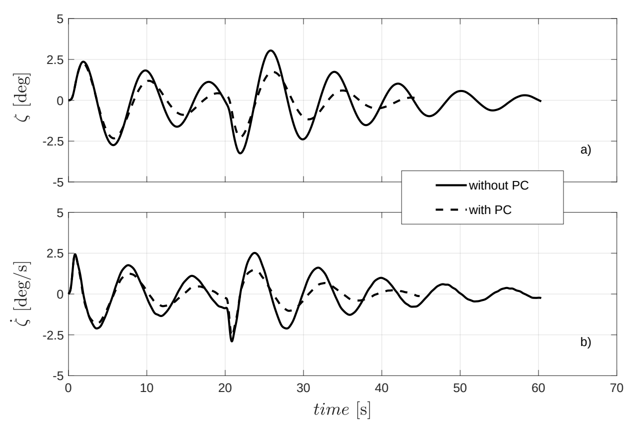

Figure 15: Case 3: stabilization of oscillation (a) angle and (b) rate with and without PC

5. CONCLUSIONS

The cooperative transportation of a payload by means of two identical rotorcraft was analyzed. First, the equations of motion were derived to describe the system made of three point–masses and two rigid cables in the presence of external disturbances. The model was then linearized about the hovering condition with the payload at rest and obtained equations were manipulated to allow the payload swing state to be observed from vehicles acceleration in the inertial frame. In this respect, a recursive algorithm, known as Fading Gaussian Deterministic Filter, was proposed to accomplish the estimation task.

Numerical validation of the approach was performed in a realistic simulation scenario where high–lifting multirotors were required to perform formation geometry–keeping, trajectory–tracking, and inter–agent collision–avoidance tasks. The estimated swing angle and rate were included in a closed–loop stabilization framework, where a suitable implementation setup was also suggested on the basis of available commercial–off–the–shelf control architectures. Active oscillation damping was shown to improve the delivery performance while determining the reduction of both maneuver time and battery power consumption in different simulation scenarios.

6. APPENDIX 1: PROOF OF THEOREM 1

The angle $\bar{\alpha}_i > 0$ between $-\boldsymbol{z}_E$ and the i–th equilibrium control force $\bar{\boldsymbol{f}}_{c_i}$ is:

$$\tan\bar{\alpha}_i = -\frac{\sqrt{\bar{f}^2_{x_{c_i}} + \bar{f}^2_{y_{c_i}}}}{\bar{f}_{z_{c_i}}} \tag{54}$$

where the tangent function can be suitably computed from force components through the $atan2$ algorithm (Ref. 43). After squaring both members of Eq. (54), one obtains

$$\bar{f}^2_{x_{c_i}} + \bar{f}^2_{y_{c_i}} - \bar{f}^2_{z_{c_i}}\,\tan^2\bar{\alpha}_i = 0 \tag{55}$$

Taking into account Eqs. (22) and (23), it is possible to recast Eq. (55) into:

$$\begin{aligned}&\left(\frac{g\,m_l\,\xi_i\,\bar{\gamma}_x}{2\sqrt{4\,L^2-\bar{\gamma}^2}} - \bar{f}_{x_{d_i}}\right)^2 \\ &\quad+\left(\frac{g\,m_l\,\xi_i\,\bar{\gamma}_y}{2\sqrt{4\,L^2-\bar{\gamma}^2}} - \bar{f}_{y_{d_i}}\right)^2 \\ &\quad-\left(-\frac{g\,M}{2} - \bar{f}_{z_{d_i}}\right)^2\,\tan^2\bar{\alpha}_i = 0\end{aligned} \tag{56}$$

Since $\xi_i^2 = 1$ and $\bar{\gamma}^2 = \bar{\gamma}_x^2 + \bar{\gamma}_y^2$, Eq. (56) is finally manipulated to obtain the polynomial expression in Eqs. (20)–(21), where payload mass m_l is collected. In the case when the agents of the formation are multirotors, $\bar{\boldsymbol{f}}_{c_i}$ is directed along $\boldsymbol{z}_{Bi}$, such that $\cos\bar{\alpha}_i$ represents the element with position $(3,\,3)$ of the direction cosine matrix $\boldsymbol{T}_{BE}(\bar{\boldsymbol{\eta}}_i)$ defined in Section 2.1. For the selected attitude representation, irrespective of set–point yaw angle $\bar{\psi}_i$, it is $\cos\bar{\alpha}_i = \cos\bar{\phi}_i\,\cos\bar{\theta}_i$, where $\bar{\phi}_i$ and $\bar{\theta}_i$ are the equilibrium roll and pitch angles, respectively (Ref. 25).

7. APPENDIX 2: ELEMENTS OF MATRICES $\boldsymbol{A}$ AND $\boldsymbol{B}$

In what follows, the elements of matrices $\boldsymbol{A}$ and $\boldsymbol{B}$ respectively defined in Eqs. (28) and (29) are listed.

$$\begin{aligned}A_{8,1} &= -\frac{g\,m_l\left(2\,M\,L^2 - m\,\bar{\gamma}_y^2\right)}{2\,m\left(2\,M\,L^2 - m\,\bar{\gamma}^2\right)\sqrt{4\,L^2-\bar{\gamma}^2}} \\ &= -A_{8,4} = -A_{11,1} = A_{11,4}\end{aligned} \tag{57}$$

$$\begin{aligned}A_{8,2} &= -\frac{g\,m_l\,\bar{\gamma}_x\,\bar{\gamma}_y}{2\left(2\,M\,L^2 - m\,\bar{\gamma}^2\right)\sqrt{4\,L^2-\bar{\gamma}^2}} = -A_{8,5} \\ &= A_{9,1} = -A_{11,2} = A_{11,5} = -A_{12,1} = A_{12,4}\end{aligned} \tag{58}$$

$$\begin{aligned}A_{8,3} &= -\frac{g\,m_l^2\,\bar{\gamma}_x\,L^2}{m\,\bar{\gamma}^2\left(2\,m_l\,L^2 + m\,\bar{\gamma}^2\right)} \\ &= -A_{8,6} = A_{11,3} = -A_{11,6}\end{aligned} \tag{59}$$

$$A_{8,7} = \frac{g\,m_l\,\bar{\gamma}_y}{2\,m\,\bar{\gamma}} = A_{11,7} \tag{60}$$

$$\begin{aligned}A_{9,2} &= -\frac{g\,m_l\left(2\,M\,L^2 - m\,\bar{\gamma}_x^2\right)}{2\,m\left(2\,M\,L^2 - m\,\bar{\gamma}^2\right)\sqrt{4\,L^2-\bar{\gamma}^2}} \\ &= -A_{9,5} = -A_{12,2} = A_{12,5}\end{aligned} \tag{61}$$

$$\begin{aligned}A_{9,3} &= -\frac{g\,m_l^2\,\bar{\gamma}_y\,L^2}{m\,\bar{\gamma}^2\left(2\,m_l\,L^2 + m\,\bar{\gamma}^2\right)} \\ &= -A_{9,6} = A_{12,3} = -A_{12,6}\end{aligned} \tag{62}$$

$$A_{9,7} = -\frac{g\,m_l\,\bar{\gamma}_x}{2\,m\,\bar{\gamma}} = A_{12,7} \tag{63}$$

$$\begin{aligned}A_{10,1} &= -\frac{g\,m_l^2\,\bar{\gamma}_x\,L^2}{m\left(4\,L^2-\bar{\gamma}^2\right)\left(2\,M\,L^2 - m\,\bar{\gamma}^2\right)} \\ &= -A_{10,4} = A_{13,1} = -A_{13,4}\end{aligned} \tag{64}$$

$$\begin{aligned}A_{10,2} &= -\frac{g\,m_l^2\,\bar{\gamma}_y\,L^2}{m\left(4\,L^2-\bar{\gamma}^2\right)\left(2\,M\,L^2 - m\,\bar{\gamma}^2\right)} \\ &= -A_{10,5} = A_{13,2} = -A_{13,5}\end{aligned} \tag{65}$$

(66) $$A_{10,3} = -\frac{g\, m_l\, M\, L^2}{m\left(2\, m_l\, L^2 + m\, \bar{\gamma}^2\right)\sqrt{4\, L^2 - \bar{\gamma}^2}} = -A_{10,6} = -A_{13,3} = A_{13,6}$$

(67) $$A_{10,7} = 0 = A_{13,7} = A_{14,1} = A_{14,2} = A_{14,3} = A_{14,4} = A_{14,5} = A_{14,6}$$

(68) $$A_{14,7} = -\frac{g\, M}{m\sqrt{4\, L^2 - \bar{\gamma}^2}}$$

(69) $$B_{8,1} = \frac{1}{m} - \frac{m_l\left(m + m_l\right) L^2\, \bar{\gamma}_x^2}{m\left[4\, m_l\, M\, L^4 + m^2\, \bar{\gamma}^2\left(4\, L^2 - \bar{\gamma}^2\right)\right]} = B_{11,4}$$

(70) $$B_{8,2} = -\frac{m_l\left(m + m_l\right) L^2\, \bar{\gamma}_x\, \bar{\gamma}_y}{m\left[4\, m_l\, M\, L^4 + m^2\, \bar{\gamma}^2\left(4\, L^2 - \bar{\gamma}^2\right)\right]} = B_{9,1} = B_{11,5} = B_{12,4}$$

(71) $$B_{8,3} = \frac{m_l\left(m + m_l\right) L^2\, \bar{\gamma}_x\sqrt{4\, L^2 - \bar{\gamma}^2}}{m\left[4\, m_l\, M\, L^4 + m^2\, \bar{\gamma}^2\left(4\, L^2 - \bar{\gamma}^2\right)\right]} = B_{10,1} = -B_{11,6} = -B_{13,4}$$

(72) $$B_{8,4} = -\frac{m_l\, \bar{\gamma}_x^2\left(2\, L^2 - \bar{\gamma}^2\right)}{2\left[4\, m_l\, M\, L^4 + m^2\, \bar{\gamma}^2\left(4\, L^2 - \bar{\gamma}^2\right)\right]} = B_{11,1}$$

(73) $$B_{8,5} = -\frac{m_l\, \bar{\gamma}_x\, \bar{\gamma}_y\left(2\, L^2 - \bar{\gamma}^2\right)}{2\left[4\, m_l\, M\, L^4 + m^2\, \bar{\gamma}^2\left(4\, L^2 - \bar{\gamma}^2\right)\right]} = B_{9,4} = B_{11,2} = B_{12,1}$$

(74) $$B_{8,6} = -\frac{m_l\, \bar{\gamma}_x\left(2\, L^2 - \bar{\gamma}^2\right)\sqrt{4\, L^2 - \bar{\gamma}^2}}{2\left[4\, m_l\, M\, L^4 + m^2\, \bar{\gamma}^2\left(4\, L^2 - \bar{\gamma}^2\right)\right]} = -B_{10,4} = -B_{11,3} = B_{13,1}$$

(75) $$B_{9,2} = \frac{1}{m} - \frac{m_l\left(m + m_l\right) L^2\, \bar{\gamma}_y^2}{m\left[4\, m_l\, M\, L^4 + m^2\, \bar{\gamma}^2\left(4\, L^2 - \bar{\gamma}^2\right)\right]} = B_{12,5}$$

(76) $$B_{9,3} = \frac{m_l\left(m + m_l\right) L^2\, \bar{\gamma}_y\sqrt{4\, L^2 - \bar{\gamma}^2}}{m\left[4\, m_l\, M\, L^4 + m^2\, \bar{\gamma}^2\left(4\, L^2 - \bar{\gamma}^2\right)\right]} = B_{10,2} = -B_{12,6} = -B_{13,5}$$

(77) $$B_{9,5} = -\frac{m_l\, \bar{\gamma}_y^2\left(2\, L^2 - \bar{\gamma}^2\right)}{2\left[4\, m_l\, M\, L^4 + m^2\, \bar{\gamma}^2\left(4\, L^2 - \bar{\gamma}^2\right)\right]} = B_{12,2}$$

(78) $$B_{9,6} = -\frac{m_l\, \bar{\gamma}_y\left(2\, L^2 - \bar{\gamma}^2\right)\sqrt{4\, L^2 - \bar{\gamma}^2}}{2\left[4\, m_l\, M\, L^4 + m^2\, \bar{\gamma}^2\left(4\, L^2 - \bar{\gamma}^2\right)\right]} = -B_{10,5} = -B_{12,3} = B_{13,2}$$

(79) $$B_{10,3} = \frac{1}{m} - \frac{m_l\left(m + m_l\right) L^2\left(4\, L^2 - \bar{\gamma}^2\right)}{m\left[4\, m_l\, M\, L^4 + m^2\, \bar{\gamma}^2\left(4\, L^2 - \bar{\gamma}^2\right)\right]} = B_{13,6}$$

(80) $$B_{10,6} = \frac{m_l\left(2\, L^2 - \bar{\gamma}^2\right)\left(4\, L^2 - \bar{\gamma}^2\right)}{2\left[4\, m_l\, M\, L^4 + m^2\, \bar{\gamma}^2\left(4\, L^2 - \bar{\gamma}^2\right)\right]} = B_{13,3}$$

(81) $$B_{14,1} = -\frac{\bar{\gamma}_y}{m\, \bar{\gamma}\sqrt{4\, L^2 - \bar{\gamma}^2}} = B_{14,4}$$

(82) $$B_{14,2} = \frac{\bar{\gamma}_x}{m\, \bar{\gamma}\sqrt{4\, L^2 - \bar{\gamma}^2}} = B_{14,5}$$

(83) $$B_{14,3} = B_{14,6} = 0$$

8. ACKNOWLEDGMENTS

This study was carried out within the MOST - Sustainable Mobility National Research Center and received funding from the European Union Next-GenerationEU (PIANO NAZIONALE DI RIPRESA E RESILIENZA (PNRR) - MISSIONE 4 COMPONENTE 2, INVESTIMENTO 1.4 - D.D. 1033 17/06/2022, CN00000023). This manuscript reflects only the authors' views and opinions, neither the European Union nor the European Commission can be considered responsible for them.

References

[1] Estevez, J., Garate, G., Lopez–Guede, J.M., Larrea, M., "Review of Aerial Transportation of Suspended–Cable Payloads with Quadrotors", *Drones* 8(35) (2024) 1–21, https://doi.org/10.3390/drones8020035

[2] Pounds, P.E.I., Bersak, D.R., Dollar, A.M., "Grasping From the Air: Hovering Capture and Load Stability", in: Proc. of IEEE Int. Conf. Robot. Autom., 2011, 2491–2498, https://doi.org/10.1109/ICRA.2011.5980314

[3] Chen, H., Quan, F., Fang, L., Zhang, S., "Aerial Grasping with a Lightweight Manipulator Based on Multi–Objective Optimization and Visual Compensation", *Sensors* 19 (2019) 4253, https://doi.org/10.3390/s19194253

[4] Eskandaripour, H., Boldsaikhan, E., "Last–Mile Drone Delivery: Past, Present, and Future", *Drones* 7(2) (2023) 1–19, https://doi.org/10.3390/drones7020077

[5] Li, X., Zhang, J., Han, J., "Trajectory planning of load transportation with multi–quadrotors based on reinforcement learning algorithm", *Aerosp. Sci. Technol.* 116 (2021) 106887, https://doi.org/10.1016/j.ast.2021.106887

[6] de Angelis, E.L., Giulietti, F., "Stability and control issues of multirotor suspended load transportation: An analytical closed–form approach", *Aerosp. Sci. Technol.* 135 (2023) 108201, https://doi.org/10.1016/j.ast.2023.108201

[7] Meissen, C., Klausen, K., Arcak, M., Fossen, T.I., Packard, A., "Passivity–based Formation Control for UAVs with a Suspended Load", *IFAC Papers Online* 50(1) (2017) 13150–13155, https://doi.org/10.1016/j.ifacol.2017.08.2169

[8] Klausen, K., Meissen, C., Fossen, T.I., Arcak, M., Johansen, T.A., "Cooperative Control for Multirotors Transporting an Unknown Suspended Load under Environmental Disturbances", *IEEE Trans. Control Syst. Technol.* 28(2) (2018) 653–660, https://doi.org/10.1109/TCST.2018.2876518

[9] Tognon, M., Gabellieri, C., Pallottino, L., Franchi, A., "Aerial Co–Manipulation With Cables: The Role of Internal Force for Equilibria, Stability, and Passivity", *IEEE Robot.* 3(3) (2018) 2577–2583, https://doi.org/10.1109/LRA.2018.2803811

[10] Pizetta, I.H.B., Brandão, A.S., Sarcinelli–Filho, M., "Avoiding obstacles in cooperative load transportation", *ISA Trans.* 91 (2019) 253–261, https://doi.org/10.1016/j.isatra.2019.01.019

[11] Costantini, E., de Angelis, E.L., Giulietti, F., "Cooperative Transportation of a Cable–Suspended Load Using Rotorcraft: A Minimal Swing Approach", in: Proc. of 49th European Rotorcraft Forum, 2023, 1–14.

[12] Masone, C., Bülthoff, H.H., Stegagno, P., "Cooperative transportation of a payload using quadrotors: a reconfigurable cable–driven parallel robot", in: Proc. of IEEE Int. Conf. Intell. Robot. Syst., 2016, 1623–1630, https://doi.org/10.1109/IROS.2016.7759262

[13] Gimenez, J., Gandolfo, D.C., Salinas, L.R., Rosales, C., Carelli, R., "Multi–objective control for cooperative payload transport with rotorcraft UAVs", *ISA Trans.* 80 (2018) 491–502, https://doi.org/10.1016/j.isatra.2018.05.022

[14] Shirani, B., Najafi, M., Izadi, I., "Cooperative load transportation using multiple UAVs", *Aerosp. Sci. Technol.* 84 (2019) 158–169, https://doi.org/10.1016/j.ast.2018.10.027

[15] Geng, J., Langelaan, J.W., "Cooperative transport of a slung load using load–leading control", *J. Guid. Control Dyn.* 43(7) (2020) 1313–1331, https://doi.org/10.2514/1.G004680

[16] Azzam, R., Boiko, I., Zweiri, Y., "Swarm Cooperative Navigation Using Centralized Training and Decentralized Execution", *Drones* 7(3) (2023) 193, https://doi.org/10.3390/drones7030193

[17] Lupashin, S., Hehn, M., Mueller, M.W., Schoellig, A.P., Sherback, M., D'Andrea, R.S., "A platform for aerial robotics research and demonstration: the flying machine arena", *Mechatronics* 24(1) (2014) 41–54, https://doi.org/10.1016/j.mechatronics.2013.11.006

[18] Zürn, M., Morton, K., Heckmann, A., McFadyen, A., Notter, S., Gonzalez, F., "MPC controlled multirotor with suspended slung load: system architecture and visual load detection", in: Proc. of IEEE Aerospace Conference, 2016, 1–11, https://doi.org/10.1109/AERO.2016.7500543

[19] Chen, T., Shan, J., "A novel cable–suspended quadrotor transportation system: From theory to experiment", *Aerosp. Sci. Technol.* 104 (2020) 105974, https://doi.org/10.1016/j.ast.2020.105974

[20] Kim, Y.S., Hong, K.S., Sul, S.K., "Anti–Sway Control of Container Cranes: Inclinometer, Observer, and State Feedback", *Int. J. Control Autom. Syst.* 2(4) (2004) 435–449, https://doi.org/10.1.1.454.9911

[21] Paul, H., Ono, K., Ladig, R., Shimonomura, K., "A Multirotor Platform Employing a Three–Axis Vertical Articulated Robotic Arm for Aerial Manipulation Tasks", in: Proc. of IEEE/ASME International Conference on Advanced Intelligent Mechatronics (AIM), 2018, 478–485, https://doi.org/10.1109/AIM.2018.8452699

[22] Dang, X., Yin, X., Zhang, Y., Gao, C., Wu, J., Liu, Y., "Improved Medium Baseline RTK Positioning Performance Based on BDS/Galileo/GPS Triple–Frequency–Only Observations", *Remote Sensing* 15(21) (2023) 5198, https://doi.org/10.3390/rs15215198

[23] de Angelis, E.L., "Swing angle estimation for multicopter slung load applications", *Aerosp. Sci. Technol.* 89 (2019) 264–274, https://doi.org/10.1016/j.ast.2019.04.014

[24] de Angelis, E.L., Giulietti, F., Rossetti, G., "Multirotor aircraft formation flight control with collision avoidance capability", *Aerosp. Sci. Technol.* 77 (2018) 733–741, https://doi.org/10.1016/j.ast.2018.04.002

[25] de Angelis, E.L., Giulietti, F., "An Improved Method for Swing State Estimation in Multirotor Slung Load Applications", *Drones* 7(11) (2023) 654, https://doi.org/10.3390/drones7110654

[26] Outeiro, P., Cardeira, C., Oliveira, P., "Control Architecture for a Quadrotor Transporting a Cable–Suspended Load of Uncertain Mass", *Drones* 7(3) (2023) 201, https://doi.org/10.3390/drones7030201

[27] PX4 Development Team and Community, PX4 Autopilot User Guide (main), <`https://docs.px4.io/main/en/`> (accessed 04/16/2024).

[28] de Ruiter, A.H.J., Damaren, C.J., Forbes, J.R., Spacecraft Dynamics and Control - An Introduction, John Wiley & Sons, Ltd., Sussex, 2013, 19–24.

[29] Li, T., Xing, H., Hashemi, E., Taghirad, H.D., Tavakoli, M., "A brief survey of observers for disturbance estimation and compensation", *Robotica* 41(12) (2023) 3818–3845, https://doi.org/10.1017/S0263574723001091

[30] Morrison, N., "Introduction to Sequential Smoothing and Prediction", 1st edition, McGraw–Hill, New York, 1969, 497–602.

[31] de Angelis, E.L., Ferrarese, G., Giulietti, F., Modenini, D., Tortora, P., "Terminal height estimation using a Fading Gaussian Deterministic filter", *Aerosp. Sci. Technol.* 55 (2016) 366–376, https://doi.org/10.1016/j.ast.2016.06.013

[32] Butcher, J.C., "Numerical methods for ordinary differential equations in the 20th century", *J. Comput. Appl. Math.* 125 (2000) 1–29, https://doi.org/10.1016/S0377-0427(00)00455-6

[33] U.S. Government Printing Office, "U.S. Standard Atmosphere", NOAA-S/T 76-1562 (1976) 1–241.

[34] Defense Mapping Agency Washington DC, "Department of Defense World Geodetic System 1984: Its Definition and Relationships with Local Geodetic Systems", 2nd edition (1991) 1–170.

[35] Najm, A.A., Ibraheem, I.K., "Nonlinear PID controller design for a 6–DOF UAV quadrotor system", *Int. J. Eng. Sci. Technol.* 22(4) (2019) 1087–1097, https://doi.org/10.1016/j.jestch.2019.02.005

[36] Rinaldi, F., Chiesa, S., Quagliotti, F., "Linear quadratic control for quadrotors UAVs dynamics and formation flight", *J. Intell. Robot. Syst.* 70(1) (2013) 203–220, https://doi.org/10.1007/s10846-012-9708-3

[37] Zhang, Y., Chen, Z., Sun, M., Zhang, X., "Trajectory tracking control of a quadrotor UAV based on sliding mode active disturbance rejection control", *Nonlinear Anal. Model Control* 24(4) (2019) 545–560, https://doi.org/10.15388/NA.2019.4.4

[38] Zhou, L., Zhang, J., Dou, J., Wen, B., "A fuzzy adaptive backstepping control based on mass observer for trajectory tracking of a quadrotor UAV", *Int. J. Adapt. Control Signal Process* 32(12) (2018) 1675–1693, https://doi.org/10.1002/acs.2937

[39] Gong, W., Li, B., Yang, Y., Ban, H., Xiao, B., "Fixed–time integral-type sliding mode control for the quadrotor UAV attitude stabilization under actuator failures", *Aerosp. Sci. Technol.* 95 (2019) 105444, https://doi.org/10.1016/j.ast.2019.105444

[40] Gao, B., Liu, Y.J., Liu, L., "Adaptive neural fault–tolerant control of a quadrotor UAV via fast terminal sliding mode", *Aerosp. Sci. Technol.* 129 (2022) 107818, https://doi.org/10.1016/j.ast.2022.107818

[41] Ogawa, S., "Robust PID Controller Tuning for Input Disturbance Rejection", *IFAC Proceedings Volumes* 30(9) (1997) 295–300, https://doi.org/10.1016/S1474-6670(17)43171-5

[42] Higham, N.J., "The Scaling and Squaring Method for the Matrix Exponential Revisited", *SIAM J. Matrix Anal. Appl.* 26(4) (2005) 1179–1193, https://doi.org/10.1137/04061101X

[43] Zhang, T., Stackhouse, P.W., Macpherson, B., Colleen–Mikovitz, J., "A solar azimuth formula that renders circumstantial treatment unnecessary without compromising mathematical rigor: Mathematical setup, application and extension of a formula based on the subsolar point and atan2 function", *Renew. Energy* 172 (2021) 1333–1340, https://doi.org/10.1016/j.renene.2021.03.047